Lateral variability in strain along a mass-transport deposit (MTD) toewall: a case study from the Makassar Strait, offshore Indonesia

Harya D. Nugraha[1,2*], Christopher A-L. Jackson[1], Howard D. Johnson[1], and David M. Hodgson[3]

[1]Basins Research Group (BRG), Department of Earth Science and Engineering, Imperial College, London SW7 2BP, UK

[2]Department of Geological Engineering, Universitas Pertamina, Jakarta 12220, Indonesia

[3]Stratigraphy Group, School of Earth and Environment, University of Leeds, Leeds LS2 9JT, UK

**Corresponding author (email: harya.nugraha14@imperial.ac.uk)*

Abstract: Contractional features characterise the toe domain of mass-transport deposits (MTDs). Their frontal geometry is typically classified as frontally-confined or frontally-emergent. However, it remains unclear how frontal emplacement style and contractional strain within an MTD can vary along strike. We use bathymetry and 3D seismic reflection data to investigate lateral variability of frontal emplacement and strain within the toe domain of the Haya Slide in the Makassar Strait. The slide originated from an anticline flank collapse, and the toe domain is characterised by a radial fold-and-thrust belt that reflects southwestwards emplacement. The frontal geometry of the slide changes laterally. In the S, it is frontally-confined, associated with a deep, *c.* 200 mbsf, and planar basal shear surface. The frontal geometry gradually changes to frontally-emergent in the W, associated with a shallow, *c.* 120 mbsf, and NE-dipping, *c.* 3°, basal shear surface. Strain analysis shows *c.* 8-14% shortening, with cumulative throw of the thrusts that increases along strike westwards from *c.* 20-40 to *c.* 40-80 m. We show that even minor horizontal translation of MTDs (*c.* 1 km) can result in marked lateral variability in frontal geometry and strain within the failed body, which may influence their seal potential in petroleum systems.

Mass-transport deposits (MTDs) are the deposits of creep, slide, slump, and debris flow processes (e.g. Dott 1963; Nardin et al. 1979; Nemec 1991; Moscardelli & Wood 2008; Posamentier & Martinsen 2011; Ogata et al. 2012). MTD emplacement can cause major geohazards for offshore infrastructures and coastal communities (e.g. Tappin et al. 2001; Vanneste et al. 2013; Takagi et al. 2019) and can be an important component of a functional petroleum system (e.g. Weimer & Shipp 2004). For example, MTDs can provide seals for hydrocarbon accumulations (Algar et al. 2011; Omeru 2014; Cardona et al. 2016) and, less commonly, may act as reservoirs (Sawyer et al. 2007; Shanmugam 2012; Arfai et al. 2016). In particular, their seal potential depends on a combination of the lithology, external geometry and internal structural heterogeneity of the emplaced mass, which are all influenced by emplacement processes (e.g. Alves et al. 2014). Thus, it is important to understand their transport processes to assess their seal potential in a petroleum system.

The nature of the failed mass in the vicinity of the toewall defines two frontal geometrical types (Frey-Martínez et al. 2006): (i) frontally-confined types characterised by a toewall that prevents a failed mass from further downdip translation, and (ii) frontally-emergent types reflecting a failed mass that extends above and beyond the toewall to translate further downdip onto the adjacent seabed. In some cases, both styles can develop within a single mass-transport event (Moernaut & De Batist 2011; Armandita et al. 2015; Clare et al. 2018). The seismic expression of both frontal termination types are well-known (Trincardi & Argnani 1990; Huvenne et al. 2002; Lastras et al. 2004; Joanne et al. 2013), but the processes occurring in the toe domain remain poorly constrained (e.g. evolution of the basal shear surface prior to termination at the toewall). Outcrop studies have provided detailed insights on processes in the toe domain, but a full 3D analysis is hindered by limited exposure extent (Martinsen & Bakken 1990; Van Der Merwe et al. 2011; Ogata et al. 2012; Sobiesiak et al. 2016; Cardona et al. 2020). Furthermore, very few studies have attempted to balance extensional and contractional strains across the entire body of an MTD (e.g. Bull & Cartwright 2019; Steventon et al. 2019). Likewise, the way in which strain varies along-strike within an MTD remains poorly understood.

Here, we use high-resolution multibeam bathymetry and high-quality 3D seismic reflection data to study the Haya Slide (hereafter the 'slide'), in the Makassar Strait, offshore western Sulawesi (Indonesia). This dataset demonstrates how frontal toewall style can change laterally during emplacement of a single mass-transport event. The bathymetry data capture the seabed expression of both the headwall and toe domains of this slide, while the 3D seismic reflection data only image the toe domain, which is the focus of this study (Fig. 1). The seismic image quality and use of seismic attributes enable us to characterise intra-MTD strain in great detail. Our specific aims are to: (i) evaluate kinematic indicators and reconstruct transport processes of the slide, (ii) assess lateral variability of the slide's frontal geometry and infer its controlling factors, (iii) quantitatively examine along-strike changes of intra-MTD strain, and (iv) discuss how lateral variations in strain may induce lateral variability of seal potential of MTDs.

GEOLOGICAL SETTING

The Makassar Strait is situated within a seismically active area, where four major plates interact (the Eurasia, Indo-Australia, Philippine Sea, and Pacific plates; Fig. 1a) (Daly et al. 1991). The strait separates the islands of Sulawesi and Borneo, and is divided into the North and South Makassar basins (Fig. 1b). A strong southwards-flowing contour current, the Indonesia Throughflow (ITF), presently carries water masses through the strait at a relatively high velocity (i.e. 1 m/s, see Fig. 1a; Mayer & Damm 2012), from the Pacific Ocean to the Indian Ocean. Brackenridge et al. (2020) suggest that the ITF preconditions the slopes bounding the Makassar Strait to fail, whereas earthquakes in this seismic-prone region may act as a trigger mechanism. More specifically, the ITF transports a high suspended sediment load southward from the Mahakam Delta, causing relatively rapid deposition and steepening of the continental slope along the western margin of the strait, which results in (i) slope oversteepening, and (ii) high pore-fluid pressures (Brackenridge et al. 2020). Such preconditioning factors for slope failure are consistent with the unusually large number of near-seabed MTDs (Pleistocene to Recent), which range in size from 5 to >600 km^3 (Brackenridge et al. 2020).

The water depth along the strait is 200-2000 m (Guntoro 1999), with (i) a relatively broad shelf area along the western margin (including the actively prograding Mahakam Delta; e.g. Allen & Chambers 1998; Roberts & Sydow 2003), and (ii) a narrower and steeper shelf along the eastern margin, which is more tectonically active and bounded by three fold-thrust belts, namely the Northern (NSP), Central (CSP) and Southern (SSP) structural provinces (see Fig. 1b; Puspita et al. 2005). These two marginal areas are the sources of the MTDs transported into the basins (Fig. 1c). The two basins are connected by the deep (*c.* 2000 m) and narrow (*c.* 45 km-wide) Labani Channel, and are cut by major structural features, such as the Palu-Koro and Paternoster transform fault zones (Cloke et al. 1999) (Fig. 1b). We here focus on the Haya Slide (Fig. 1d); this is located *c.* 10 km off the coast of Sulawesi, at the southern end of the Labani Channel, close to the southern margin of the SSP (Fig. 1b). The slide is a shallowly buried MTD with only a thin (<8 m) cover of modern sediment and a clear present-day seabed expression.

DATA SET AND METHODOLOGY

Data set

The study is based primarily on bathymetry, 3D seismic reflection and well data (Fig. 1b and d). TGS provided the multibeam echosounder bathymetry data (TGS_Pat survey), which covers an area of *c.* 20,000 km^2. Lateral resolution of these data is 25 x 25 m and geomorphic features are enhanced by a shaded relief map with 0^o azimuth and 45^o angle. Core descriptions of near-seabed sediments (*c.* 3-7 mbsf) are also available (i.e. TGS009 and TGS194, see Fig. 1b). Although none of these cores directly sample the Haya Slide, they enable the likely lithology of the slide to be inferred.

The post-stack time-migrated (PSTM) 3D seismic reflection and exploration well data (see Fig. 1b) are provided by the Information and Data Centre, Ministry of Energy and Mineral Resources (PUSDATIN ESDM), Indonesia. The seismic reflection data cover an area of 1598 km^2**,** with a bin spacing of 25 m x 12.5 m (inline x crossline) and a dominant frequency of 50 Hz at the base of the Haya Slide (*c.* 200 mbsf). We estimate that the spatial resolution of the seismic data, given an average velocity of the sedimentary package of interest derived from the wells (1495 m/s), is *c.* 7 m. The average velocity of the near-seabed sediments is relatively low, likely due to the high water content. Similar values are obtained for near-seabed, deep-water sediments penetrated in the South Makassar MTC area, which is located *c.* 135 km to the SW of our study area (see Fig. 1b; Armandita et al. 2015). The 3D seismic data are zero-phase with SEG normal polarity with an increase in acoustic impedance expressed as a positive amplitude.

The two wells (XR-1 and XS-1) do not penetrate the Haya Slide, and there are no drill cuttings data available, even within the general stratigraphic interval containing the slide. However, the correlation of the basal shear surface to the XR-1 and XS-1 wells (see 'detachment level' in Fig. 1d) enables the velocity of the sedimentary package containing the slide to be inferred. Using these data allows the conversion of measured vertical distances from time (ms TWT) to depth (m).

The bathymetry data allow delineation of the external geometry of the slide (Fig. 2). These data also allow the headwall and a lateral margin (Eastern Lateral Margin, Fig. 2) of the slide to be determined (not covered by the 3D seismic reflection data).

Seismic interpretation

The 3D seismic reflection data cover most of the toe domain of the slide (Figs. 2 and 3). Mapping of the seabed and basal shear surface of the slide enables us to constrain the structural style of its toe domain and infer the emplacement processes of the slide. Two seismic attributes were used to visualise the range of intra-MTD structures. First, variance was used to enhance discontinuities such as imbricated thrusts (e.g. Chopra & Marfurt 2007). Second, spectral decomposition (RGB blending) was conducted to highlight heterogeneities of internal body of the slide, by blending three bins of frequency volume with assigned colours (i.e. red, green and blue represent low, mid and high frequencies, respectively) (e.g. Partyka et al. 1999; Eckersley et al. 2018). We extracted these attributes along an isoproportional slice, i.e. proportionally located halfway between the seabed and the basal shear surface (see Zeng et al. 1998), and horizontal time-slices, thereby generating map-view images of seismic facies and structural variability (e.g. Fig. 3b).

Strain analysis

Shortening calculation

We calculate shortening and investigate longitudinal strain distribution within the toe domain of the Haya Slide by using the well-established line-length method (Dahlstrom 1969; Totake et al. 2018; Bull & Cartwright 2019; Steventon et al. 2019). We selected a representative depth-converted seismic section that is parallel to the dominant transport direction of the slide (Figs. 3b and 4a). This was determined based on the analysis of kinematic indicators, including the trend of the lateral margin and fold-and-thrust belt (e.g. Bull et al. 2009). Shortening values (e) of faulted and folded pre-kinematic strata are estimated by comparing the present length (L_f) with the cumulative length of the faulted and folded pre-kinematic horizon (L_i) (Eq. 1).

$$e = (L_f - L_i)/L_i \tag{1}$$

However, the estimated shortening values from this line-length method provides only a minimum value, since it does not account for shortening within pop-up blocks due to sub-seismic strain, and lateral compaction accommodated by porosity loss via dewatering and/or grain crushing (Moore et al. 2011; Armandita et al. 2015; Alsop et al. 2019; Steventon et al. 2019).

Along-strike strain analysis

As contractional features (e.g. thrusts, and thrust-bound pop-up blocks) in the toe domain of the slide are highly segmented along-strike, we focus on a contractional feature where a pre-kinematic horizon can be interpreted over the longest along-strike distance. We measured throw along the strike of internal and bounding thrust faults of the contractional pop-up blocks at intervals of 20-200 m. As most of the thrust faults dip steeply (40°-60°), we quantify fault displacement by measuring throw rather than heave. This is because the heave of steeply-dipping thrusts diminishes with increasing dip (Totake et al. 2018). We then plot throw against along-strike distance.

RESULTS AND INTERPRETATION

General characteristics of the Haya Slide

External geometry and lithological composition

The Haya Slide is *c.* 16 km long, extending southwestwards from the lower slope (*c.* 1700 m below sea-level) to the basin floor (*c.* 2000 mbsl). The slide has a lobate geometry (Fig. 2): (i) it is *c.* 7 km-wide in its headwall region on the lower slope, (ii) widens to *c.* 15 km along its frontal margin in the centre of the basin floor, and (iii) covers an area of 150 km^2. The slide was derived from the southern flank of a thrust-cored anticline within the SSP (Figs. 1 and 2). The anticline has a broadly arcuate trend and is dissected by the headwall of the slide, extending from 1700 to 1900 mbsl (Fig. 2). The external limits of the slide are defined as follows (Fig. 2): (i) Northern Lateral Margin, (ii) Eastern Lateral Margin, and (iii) Frontal Margin. This external geometry, and the position of the headwall of the slide, indicates that the slide was emplaced towards the SW.

Correlation with the laterally equivalent, slide-hosting package in wells XR-1 and XS-1 (Fig. 1d), confirms that the slide is located stratigraphically within the Quaternary. Cores from the slope (TGS009) and basin floor (TGS194) locations (Fig. 1b) indicate that: (i) slope sediments are composed of argillaceous (fine to medium) sand, with low-medium cohesion and medium-high water content, and (ii) basin floor sediments are characterised by very soft to firm clay, with medium cohesion and medium-high water content.

Thickness variation and area sub-division

The 3D seismic reflection data cover *c.* 78% of the slide, mainly covering its downdip portion and excluding the headwall region (see inset map in Fig. 3a). Thickness patterns (Fig. 3a) and frequency characteristics (Fig. 3b) display gradual variations in both strike and dip directions, which enable subdivision of the slide. Strike-oriented thickness variations highlight three distinct areas (Fig. 3a): (i) A (*c.* 170-200 m thick), (ii) B (*c.* 140-170 m), and (iii) C (*c.* 70-140 m). All three areas thin and wedge-out abruptly downdip, at approximately the same rate, towards the Frontal Margin. Area C also thins abruptly along strike, at a similar rate, towards the Northern Lateral Margin that represents a boundary separating the downslope-translating slide and stationary substrate. The Eastern Lateral Margin is inferred using bathymetry data alone, whereas the Northern Lateral Margin is imaged directly by the 3D seismic reflection data.

Description of MTD seismic facies

Dip-oriented variations are defined by an isoproportional slice, taken midway between the basal shear surface and seabed (Fig. 3b), which shows frequency changes indicative of seismic facies and/or structural variability. The inner part of the slide is characterised by an overall lower RGB blend frequency and relatively short, discontinuous along-strike lineations. In contrast, outer areas display higher RGB blend frequency with longer, more continuous lineations, which extend across Areas A-C (Fig. 3b). These lineations predominantly trend E (090-270°) in the S (Area A) and N to NW (000-180°, 020-200°) in the W (Area C).

Three dip-oriented seismic sections across Areas A, B and C, oriented perpendicular to the curved lineations (Fig. 3b), define the internal character of the slide (Fig. 4a-c). These sections show that the inner part of the slide comprises chaotic, highly discontinuous, low-amplitudes reflections, which corresponds to the low RGB blend frequency seen in the spectral decomposition map (Fig. 3b). Between the inner and outer parts, we observe isolated, high RGB blend frequency bodies (Fig. 3b). These bodies correlate with isolated, folded, high-amplitude reflections encased within the background chaotic and transparent reflections (Fig. 4a-c). The more continuous curved lineations in the outer part of the slide (Fig. 3b) correspond to pairs of sharp discontinuities within the slide (Figs. 4a-c). These discontinuities converge downward onto the basal shear surface and mark the boundary between folded and relatively horizontal reflections (e.g. Fig. 4a).

In map-view, there are also 20 to 65 km-long, 50 to 150 m-wide curved discontinuities extending mainly within the outer part (see white dotted lines in Fig. 3b). These discontinuities crosscut the high RGB blend frequency bodies, and orientated oblique, and become sub-parallel downslope, to the continuous lineations bounding the bodies (Fig. 3b).

Interpretation of MTD seismic facies

The seismic expression of the inner part (low RGB blend frequency with predominantly chaotic and transparent reflections) is typical of an internally disorganised and highly deformed debrite, as compared to other, drilled examples of MTDs (e.g. Piper et al. 1997; Posamentier & Martinsen 2011). The isolated bodies between the inner and outer parts are interpreted as megaclasts, with their long axes oriented sub-parallel to the curved lineations (Jackson 2011; Alves 2015; Gamboa & Alves 2015; Hodgson et al. 2018; Sobiesiak et al. 2018; Sobiesiak et al. 2019).

The continuous lineations in map-view (Fig. 3b) corresponding to reflection discontinuities in seismic sections (Figs. 4a-c), are interpreted as forethrusts (i.e. NE-dipping) and backthrusts (SW-dipping). These thrusts bound the high RGB blend frequency bodies (in map-view, see Fig. 3b) that correspond to the folded reflections in their hangingwalls (in seismic sections, e.g. Fig 4a). These bodies are interpreted as 'pop-up blocks' (e.g. Frey-Martínez et al. 2006; Bull & Cartwright 2019).

The pop-up blocks are crosscut along-strike by the curved discontinuities that trend oblique to them upslope and become sub-parallel downslope (see white dotted lines in Fig. 3b). These discontinuities are interpreted as sub-orthogonal shear zones (*sensu* Steventon et al. 2019) that may record boundaries between different flow cells that moved at different speed within the translating failed mass (e.g. Masson et al. 1993; Steventon et al. 2019). This differential speed might be induced by intermittent deceleration of flow cells, as shearing along the shear zones halted when they merged downslope with the thrusts at different times (Fig. 3b) (e.g. Steventon et al. 2019). Therefore, these shear zones represent strike-slip movement between flow cells. Due to the predominantly sub-orthogonal orientation relative to the dominant transport direction, the shear zones are not interpreted as longitudinal shear zones (*sensu* Bull et al. 2009). This is because the longitudinal shear zones are orientated sub-parallel to the local transport direction (Masson et al. 1993; Gee et al. 2005; Bull et al. 2009; Steventon et al. 2019).

Although thrust-bound pop-up blocks typify the outer part of the slide, there are significant lateral variations (from Area A to Area C) in structural style and seismic facies characteristics, which are described below.

Area A

Characteristics of Area A

A gradual downslope-deepening of the basal shear surface characterises the base of the slide in Area A. The surface steps up to form a steep ramp (*c.* 60°) that defines the slide's frontal margin (Fig. 4a). The basal shear surface is deepest (*c.* 200 mbsf) adjacent to the frontal margin, with the basal shear surface essentially being horizontal. The upper surface of the slide is of low relief in the inner part, and it becomes more rugose down-dip and reaches its highest relief (15 m) at the frontal margin.

Seismic reflections in the outer part of the slide in Area A are well-imaged and can be directly correlated with undeformed strata beyond the frontal margin, despite being contractionally offset by thrust faults (Fig. 4a). The internal reflections of the slide become more irregular, and harder to trace, towards the inner part. In area A, the average throw and dip of the fore- and backthrusts are *c.* 30 m and *c.* 45°, respectively, with the spacing between thrust pairs (measured from crest to crest of pop-up blocks) ranging from 400 to 500 m.

Interpretation of Area A

The steep frontal ramp that separates undeformed basin-floor strata from the slide is a classic frontally-confined (*sensu* Frey-Martínez et al. 2006) termination style (Fig. 4a). In the inner part, the low seabed relief may partly reflect the infilling of the slide's top-surface relief by post-emplacement sedimentation (ponded sediments in Fig. 4a). In the outer part, the thickness of the slide (*c.* 200 m) is only expressed by minimal seabed relief at the edge of the deposit (*c.* 15 m), similar to previously documented frontally-confined MTDs (e.g. Lastras et al. 2004; Frey-Martinez et al. 2005).

Internal reflections show higher preservation of stratal reflections in the outer than the inner parts, suggesting that the youngest thrust is located at the frontal margin of the slide (Fig. 4a), similar to those observed from outcrops (e.g. Alsop et al. 2019) and seismic reflection data (e.g. Frey-Martínez et al. 2006; Bull & Cartwright 2019). Physical modelling results suggest that regular spacing of fore- and backthrusts is indicative of an MTD that was translated on a low friction basal shear surface (Huiqi et al. 1992).

Area B

Characteristics of Area B

The basal shear surface in Area B progressively steps up through stratigraphy to define a ramp-flat-ramp structural configuration (Fig. 3a and Fig. 4b). The basal shear surface is deepest (*c.* 170 mbsf) immediately upslope from the first and deepest frontal ramp with the highest relief (30 m). The other two ramps are more gently-dipping and have lower relief (*c.* 20 m) (Fig. 4b). These three ramps truncate otherwise continuous, sub-parallel reflections defining the pre-slide substrate (i.e. composed of moderately cohesive clay). The substrate in Area B dips very gently (*c.* 1^{o}) in an opposing direction (i.e. northeastwards) to the slide transport direction. The seabed in Area B is smooth but becomes more rugose downdip (Fig. 4b). Most notably, the highest seabed relief (*c.* 10 m) is located immediately above the deepest point of the basal shear surface.

The nature and distribution of the seismic facies in Area B differs from those of Area A, which are characterised by a much higher level of reflection discontinuity. Also, the least disturbed strata (i.e. semi-continuous seismic reflections) occur in the central part of the slide, immediately upslope from the first frontal ramp. Directly above the frontal ramps, reflections are extremely chaotic with variable, higher amplitude seismic facies encased within more extensive transparent seismic intervals, which resemble those in the inner part (Fig. 4b).

In the central area, where stratal reflections have the highest preservation, pop-up blocks and thrusts are geometrically similar to those in Area A (Fig. 4b). However, these pop-up blocks have a spacing of *c.* 150-300 m, which is about half that of Area A. Measuring the throw and dip of thrusts in Area B is harder than in Area A, due to more chaotic arrangement of internal reflections. The continuous nature of pop-up blocks and thrusts in map-view (Fig. 3b), however, suggest that the more chaotic arrangement in seismic sections is likely due to seismic resolution limitations and the closer spacing of the thrusts. Where we can trace a marker horizon between thrust-bound pop-ups, the throw and dip of the thrusts are 49 m and 60º, respectively (i.e. similar to the maximum values observed in Area A).

A distinctive upstanding, undeformed block is identified on a variance time-slice and seismic section (see 'Intact block' in Fig. 5), which marks the transition between Area A and B. This block extends gradationally downwards into the undeformed slope-to-basin floor strata (Fig. 5b), which continue unbroken towards the E (Fig. 5a). The block is bound in the N by the steep frontal ramp defining Area A and pop-up blocks within the toe domain of the slide (in the W and S). The block is capped by sub-parallel, variable-amplitude reflections, while in the S it is bound by folded reflections that are cross-cut by minor thrusts. These thrusts detach onto a reflection that is stratigraphically shallower than the basal shear surface within the slide's main body (Fig. 5b).

Interpretation of Area B

The stepped geometry of the basal shear surface confining the slide in Area B argues against frontal emergence of the slide (Frey-Martínez et al. 2006). Seismic facies above the stepped frontal ramp comprise variable-amplitude, somewhat chaotic reflections that resemble debrites (*cf.* Posamentier & Kolla 2003; Ortiz-Karpf et al. 2017) (Fig. 4b). Pop-up blocks in Area B are located immediately updip from the frontal ramps (Fig. 4b). Here, the slide is thinner, and it contains more closely-spaced pop-up blocks than those in Area A. We therefore speculate that there might be a relationship between thickness and pop-up block width/thrust fault spacing. This is consistent with the physical and numerical modelling by Liu & Dixon (1995), who demonstrate a positive linear relationship between thrust spacing and thickness of the strata.

The intact block (i.e. composed of continuous reflections) can consistently be separated from folded and discontinuous reflections above and to the sides of the block (Fig. 5b). Therefore, we suggest that the basal shear surface steps up above this block, before stepping down to the reflection onto which the minor thrusts detach (Fig. 5b). The surface then steps up again to define the outermost frontal margin in Area B. Beyond this outermost frontal margin, a gently folded reflection is observed that probably marks the position where the next thrust would have formed (Frey-Martínez et al. 2006).

We interpret the intact block as a piece of *in situ* substrate, based on its lack of deformation and gradational seismic facies relationship with underlying and adjacent basin floor strata. Hence, it can be interpreted as a remnant block (*sensu* Bull et al. 2009). The minor thrusts downdip from the remnant block suggest that there is a zone of relatively high strain beyond the main body of the slide (Fig. 5b). This zone of high strain could be a distributed shear zone, where compressional stress is transmitted beyond the frontal ramp (Hodgson et al. 2018). However, in those cases, the distributed shear zone is commonly in direct contact with the frontal margin of the main body (e.g. Watt et al. 2012).

In our case, the remnant block exists in between two zones of relatively high strain (Fig. 5b). Therefore, an alternative interpretation is that the minor thrusts represent the lateral propagation of thrusts eastwards from Area C (Fig. 5a). This interpretation is plausible given that minor thrusts can be traced westwards on the variance time-slice, towards the main body of the slide (i.e. into Area C, Fig. 5a). The relationship between the main body of the slide, the remnant block, and the minor thrusts, partially resemble a process referred to as 'enveloping' (Hodgson et al. 2018). For example, a remnant block could form when an uneven frontal margin to the slide envelopes a large piece of substrate, but with the process terminating prior to complete entrainment of the block due to cessation of the slide's translation.

Area C

Characteristics of Area C

The basal shear surface in the outer part of Area C exhibits a similar geometry and internal characteristics to that of Area B, especially the staircase-like geometry of the basal shear surface (Fig. 4c). However, the basal shear surface here is associated with a pronounced change in dip and dip direction, defined by a change from *c.* 1^{o} basinward dip to a *c.* 3^{o} landward dip (Figs. 4c and 6a). This change in dip coincides with the deepest (120 mbsf) occurrence of the basal shear surface. The seabed in Area C is characterised by a (i) *c.* 10 m vertical relief, and (ii) a *c.* 6 km long and 2 km wide 'bulge', immediately updip of the slide's frontal margin (Figs. 4c, 6b-c). Adjacent to the Northern Lateral Margin, the basal shear surface is relatively flat, and the seabed shows rugosity similar to that in Areas A and B, but with a shorter wavelength (Fig. 6d).

The internal characteristics of the slide in Area C, which resemble those in Area B, comprise the following: (i) chaotic reflections of variable amplitude encased within very low-amplitude reflections at the frontal margin, (ii) pop-up blocks within the slide's outer part, and (iii) megaclast-bearing debrites in the inner part (Fig. 4c). However, the pop-up blocks in Area C are more closely spaced (*c.* 100-150 m) than those in Area B, which results in low stratal preservation in seismic sections (Fig. 4c). Thus, despite being well-imaged in map-view, from which pop-up blocks spacing can be measured (Fig. 3b), dip and throw measurements in Area C are uncertain (Fig. 4c).

The frontal margin in Area C is characterised by rapid pinch-out of the slide's internal body onto the inclined (*c.* 3^{o}) substrate (Fig. 4c). Towards the Northern Lateral Margin, the spacing between pop-up blocks is even shorter (*c.* 70-100 m), and the basal shear surface is shallower (70 mbsf) (Figs. 3 and 6d).

Near the frontal margin, sub-parallel, discontinuous, high-amplitude reflections occur between the basal shear surface and the largely transparent seismic facies defining the main body of the slide (Fig. 4c). These reflections are identical, thus could be directly correlated, to the reflections within a *c.* 25

m-thick interval located basinward of the slide, comprising inclined, largely undeformed, reflections (Fig. 4c).

The boundary between Areas B and C comprises a NE-trending/NW-facing ramp, which is laterally continuous with the NW-trending/NE-facing frontal ramp of Area B (Fig. 7a). Variance attributes extracted from a 50 ms TWT thick window above the basal shear surface show several NW-trending lineations that terminate against the NE-trending ramp. In seismic section, these lineations correspond to fold-and-thrust belt structures in Area C (Fig. 7b). Thus, the NE-trending ramp forms a boundary between the fold-and-thrust system and the undeformed substrate. The NE-trending ramp also coincides with a positive relief on the seabed.

Interpretation of Area C

The slope gradient break at the basal shear surface and emergent of the leading-edge part of the slide that onlaps onto the underlying inclined substrate are likely to be related. We suggest that the physical impact of the downslope-translating slide onto its substrate was highest where the basal shear surface abruptly changes dip and dip direction (Ogata et al. 2014b). Following this impact, variations in the mechanical properties of the substrate likely controlled the morphology of the basal shear surface (Strachan 2002; Frey-Martinez et al. 2005; Moernaut & De Batist 2011). For instance, substrates with higher shear strengths (e.g. due to lower pore-pressure) force the basal shear surface to step-up to shallower substrates and propagate along inclined substrates that have lower shear strength (Fig. 4c). The inclined basal shear surface and momentum gained by the slide at the dip change provide sufficient inertial energy for the translating mass to abandon the basal shear surface and emerge onto the coeval basin floor, and to onlap the bathymetric high (Figs. 4c, 6b) (Frey-Martinez et al. 2005; Frey-Martínez et al. 2006). Therefore, we classify the slide in Area C as frontally-emergent (*sensu* Frey-Martinez et al. 2006). However, the slide also becomes frontally-confined adjacent to the Northern Lateral Margin, where the slide is thin, and the basal shear surface is relatively flat and lacks a distinct dip change (Fig. 6d; *cf.* Area A in Fig. 4a).

The abrupt change in basal shear surface dip has at least two additional consequences. Firstly, the internal body of the slide was likely disaggregated due to the buttressing effect of the underlying substrate (Mandl & Crans 1981). This resulted in the partially-disaggregated debrite facies in the frontal margin area, which is manifested as the broad bulge on the seabed (Fig. 6b-c). Secondly, the impact of the translating mass onto the substrate develops a zone of stratigraphically parallel, discontinuous reflections directly on top of the basal shear surface (e.g. Joanne et al. 2013; Hodgson et al. 2018; Sobiesiak et al. 2018; Steventon et al. 2019). We interpret these reflections as lying within the basal shear zone, in which the substrate was deformed due to compressional forces exerted by the slide, but was not fully entrained (e.g. Joanne et al. 2013; Festa et al. 2016; Hodgson et al. 2018; Sobiesiak et al. 2018; Ogata et al. 2019; Cardona et al. 2020).

The abrupt boundary between Areas B and C indicates that the basal shear surface evolved differently between the two areas, where the frontal ramp of Area B was cross-cut by the main body in Area C (Fig. 7a). This cross-cutting relationship probably formed by the slide's erosion of the substrate in Area C, which formed the NW-facing ramp (Fig. 7a-b). Lateral variations in basal shear surface growth and geometry could also be related to lateral variations in the mechanical properties of the stratigraphy overlying the basal shear surface (e.g. permeability, pore-pressure and related shear strength). In addition, variations in the magnitude of stress exerted by the slide onto, and into, the substrate in adjacent areas may have occurred (Strachan 2002; Frey-Martinez et al. 2005). Positive seabed relief adjacent to the NE-trending ramp likely reflects a buttressing effect of the main body of the slide against the ramp as new material was entrained by the slide (Fig. 7b).

Strain distribution in the toe domain

We here estimate the translation distance of the Haya Slide based on an assessment of shortening within Area A that has the best preservation of internal reflections. We also quantify intra-MTD strain of a pop-up block within Area A to investigate how strain varies along strike.

Shortening and vertical strain variability

The distance travelled by the slide can be estimated by measuring total shortening in the frontally-confined part of toe domain, as long as the fold-and-thrust belts and the internal reflections are well-preserved and imaged (*cf*. Frey-Martínez et al. 2006; Bull & Cartwright 2019). However, we note that the calculated translation distance here is a first-degree estimation of how far the slide has travelled in the toe domain (Frey-Martínez et al. 2006), and, thus, it does not represent run-out distance, which is measured from the headwall to the leading-edge of the deposit (Clare et al. 2018).

A representative depth-converted seismic-section in Area A (interval velocity derived from wells XR-1 and XS-1) was selected for our shortening calculation based on line-length method (see Figs. 3b and 4a). This section is orientated perpendicular to the strike of the fold-and-thrust belt, and stratal reflections within individual thrust-bound blocks are well-imaged, and can thus be interpreted with confidence. Two intra-MTD horizons were interpreted (H1-2, see Fig. 4a) to better constrain the amount of horizontal shortening and to determine how this varies vertically. These horizons extend from undeformed basin-floor strata to the updip limit of the outer part (Fig. 4a).

The present and restored lengths of H1, the deepest horizon, are 6.73 km and 7.79 km, respectively, which equate to 14% contraction (1.06 km). In contrast, the shallower H2 horizon experienced only 8% contraction (0.61 km), derived from present and initial lengths of 6.65 km and 7.26 km, respectively. This analysis shows two key results: (i) contractional structures in Area A (Fig. 4a) formed in response to horizontal translation of the slide over a relatively short distance (0.61-1.06 km), and (ii) greater contraction of the deeper H1 horizon compared to the shallower H2 indicates depth-dependent layer shortening, which is explained further below.

Along-strike strain variability

An along-strike analysis enables the kinematics behind the spatial configuration of fold-and-thrust belts to be assessed (Dahlstrom 1969). Such studies have been performed for kilometre-scale, deep-water fold-and-thrust belts using 3D seismic reflection data (e.g. Higgins et al. 2009; Totake et al.

2018). Here, we document the along-strike variability of intra-MTD strain at a significantly smaller-scale, but exceptionally well-imaged, fold-thrust system within the Haya Slide.

We conducted the along-strike analysis on Pop-up Block 3 (i.e. the third block counted from the frontal margin, and herein referred to as PB-3; see Fig. 4a) and its associated fore- and backthrusts. This pop-up block is ideal for this analysis because its main bounding thrust fault (FT-1) and Horizon H2 can be interpreted over the longest distance (*c.* 3 km along strike, see Fig. 8a); other pop-up blocks are shorter and more segmented along strike (*c.* 0.5-1 km).

Structural configuration in map view. Mapping of H2 laterally from the representative section of Area A (i.e. Fig. 4a) reveals a more complicated configuration of pop-up structures associated with PB-3; whereas there is only a single pop-up in the E (PB-3a), there are two in the W (PB-3b-c; Fig. 8a). These three pop-up blocks are readily identified on a variance time-slice (Fig. 8b). Here, one of the sub-orthogonal shear zones identified in the previous section (see General Characteristics and white dotted lines in Fig. 3b), trends oblique to, and cross-cuts, the thrust faults near the central part of the focused study area (white dotted line in Fig. 8b). This shear zone clearly defines the boundary between PB-3a in the E (i.e. eastern domain) and PB-3b and c in the W (i.e. western domain, see Fig. 8a). At this shear zone, the southern margin of the PB-3a and b shows an 80 m left-lateral (sinistral) offset (Fig. 8b).

PB-3a is bound on its northern margin by one major backthrust (BT-1), and one minor FT-2 exists adjacent to FT-1. In contrast, PB-3b is bound on its northern side by BT-2 and -3 that forms a 'soft-linkage' with each other (*sensu* Walsh & Watterson 1991). Unlike PB-3a and -b, PB-3c is not bound by FT-1, but is instead bound by two forethrusts (FT-4 and FT-5) and two backthrusts (BT-4 and BT-5). BT-1 and BT-4 are soft-linked (near the shear zone) and bound the northern margin of PB-3a and c, respectively (Fig. 8a). The faults bounding the three pop-up structures generally strike E-W to ESE-WNW. In addition to the faults that define PB-3a-c, we identify two faults (i.e. FT-3 and BT-6) within the shear zone that bound a narrow (*c.* 100 m-wide), high-relief (*c.* 20 m-high) block (Fig. 8a-b).

Throw profiles. An along-strike throw projection of individual fore- and backthrust faults shows irregular shapes of throw profiles (Fig. 8c). T-x plot of FT-1 shows a slightly bimodal throw profile, where it has a slightly lower throw (*c.* 5-10 m) in the western (PB-3b) than in the eastern (PB-3a) domains (Fig. 8c). This contrasts with an increase of the number of thrusts in the western domain, resulting in a significantly higher cumulative throw: from *c.* 20-40 m in the E to *c.* 40-80 m in the W (Fig. 8c). A local minimum in the cumulative throw profile, which coincides with the local minima of FT-3, marks the boundary between the eastern and western domains (Fig. 8c). The seismic sections across PB-3 depict the change in the fold-and-thrust configuration along strike (Fig. 8d-f), from the eastern area, across the shear zone, to the western area.

Interpretation. We interpret the two different strain domains within the translated mass (i.e. the eastern and western domains, see Fig. 8a-b), separated by an intra-MTD, syn-emplacement shear zone (i.e. the sub-orthogonal shear zone described in General Characteristics and highlighted by the white dotted lines in Fig. 3b). These two domains were likely transported a similar distance. This is because the western domain appeared to travel downdip only a small amount further than the eastern domain (i.e. 80 m) when compared to the overall estimated translation distance of the slide (i.e. 8-14% of 0.61-1.06 km translation distance). There are also more thrusts in the western than the eastern domains (Fig. 8a-b). Between the two domains, the narrow and high-relief block is interpreted as an uplifted block that may have formed due to transpression within the shear zone (Sanderson & Marchini 1984).

The throw profiles of the individual fore- and back-thrusts resemble larger, tectonic-scale fold-thrust systems, such as the compressional tectonics in offshore NW Borneo (Totake et al. 2018) and the gravitational tectonics of the Niger Delta (Higgins et al. 2009). The markedly higher cumulative throw of the western domain, as compared to the eastern domain, implies that the western domain experienced markedly different amounts of contraction (Fig. 8c). This might indicate that pop-up structures in the western domain are in a more advanced phase of growth (e.g. Cartwright et al. 1995; Totake et al. 2018). The local minima in the cumulative throw profile may represent a paleo-linkage site (Ellis & Dunlap 1988), which in this study coincides with the shear zone (Fig. 8a-b). Hence, the shear zone not only reflects differential timing or velocities of translating masses within an MTD (Masson et al. 1993; Bull et al. 2009; Steventon et al. 2019), but it could also separate two translating masses recording different amounts of strain, despite being translated for a similar distance.

DISCUSSION

We here discuss the slide transport processes and lateral variability of frontal emplacement and intra-MTD strain within the toe domain. Also, we discuss the implications for assessing the seal potential of MTDs in relation to hydrocarbon accumulations.

Modes of transport

Frey-Martínez et al. (2006) show the headwall domain of frontally-confined MTDs are defined by internally coherent, normal fault-bound blocks. In this domain, there is only limited depletion of the failed mass immediately downdip of the headwall. However, more recent studies show that major sediment depletion in the headwall domain can occur even if the MTDs are frontally confined (e.g. Lastras et al. 2004; Watt et al. 2012; Joanne et al. 2013). In such cases, these frontally-confined MTDs are generally characterised by strongly disaggregated, debritic material in their inner parts, rather than fault-bound blocks. Downdip, contractional structures (e.g. folds and imbricated thrusts) display increasing stratal preservation distally.

The Haya Slide comprises an inner, debrite-dominated part and an outer part dominated by contractional structures. The debrite likely originated from the collapse of the southern flank of an updip anticline (see Fig. 3). This deformed the seabed and entrained the substrate (Fig. 9a), which resulted in flow bulking further downslope (Gee et al. 2001; Gee et al. 2007; Butler & McCaffrey 2010; Ogata et al. 2019). Substrate entrainment and subsequent downslope translation then produced transparent seismic facies (i.e. the debrite in Fig. 4), indicating that the incorporated material was increasingly disaggregated (Posamentier & Kolla 2003; Ortiz-Karpf et al. 2017). Erosion and disaggregation by the debris flow continued until the shear stress exerted by the flow was unable to entrain more substrate (Fig. 9b). At this point, the debris flow applied significant shear and compressional stress (lateral loading) to the substrate ahead of, and to the sides of, the flow (Butler & McCaffrey 2010; Hodgson et al. 2018).

The strata ahead of the debris flow were translated a short distance (i.e. 0.61-1.06 km), forming broadly symmetrical pairs of fore- and backthrusts (Fig. 9c). This symmetrical geometry of the thrusts is likely due to horizontal buckling on a low friction basal surface during shearing (Huiqi et al. 1992). The low basal friction may reflect the fact that the failed mass was translating on high-water content substrate with high pore pressure (e.g. Armandita et al. 2015). The two styles of MTD-substrate interactions, i.e. erosion and deformation (Fig. 9c), have been documented elsewhere, both in seismic reflection (e.g. Schnellmann et al. 2005; Watt et al. 2012; Joanne et al. 2013; Ogata et al. 2014a; Bull & Cartwright 2019; Omeru & Cartwright 2019; Steventon et al. 2019), and field data (Van Der Merwe et al. 2011; Ogata et al. 2012; Ogata et al. 2014b; Festa et al. 2016; Sobiesiak et al. 2016; Hodgson et al. 2018; Ogata et al. 2019; Sobiesiak et al. 2019; Cardona et al. 2020). Adjacent to the toewall, the basal shear surface exhibits different geometries along strike (Fig. 10). This along-strike variability will be discussed in the following section.

Lateral variability of the toe domain

Lateral variability of frontal confinement

Moernaut & De Batist (2011) investigated sub-lacustrine MTDs to understand what controls whether an MTD remains confined, or whether it abandons its basal shear surface and emerges onto the coeval basin floor. They conclude that the drop height and depth of the basal shear surface are the main factors controlling frontal emplacement style. The former represents a driving force (i.e. gravitational potential energy), and the latter represents a resisting force (i.e. potential energy needed to be exceeded for the MTD to emerge).

The Haya Slide originated from a headwall at a depth of *c.* 1700 mbsl, and its frontal margin is at *c.* 2000 mbsl (the basinward extent of Areas A to C) (see Fig. 3). Thus, the drop height of the slide is 300 m, which provided a similar driving force (potential energy) for all the three frontal areas. However, the depth of the basal shear surface, and thus the thickness of the slide, varies laterally: it is deepest in Area A (*c.* 200 mbsf) and shallowest in Area C (*c.* 120 mbsf). This lateral variability of basal shear surface depth, slide thickness and degree of confinement must also reflect lateral changes in the ratio between the resisting and driving forces (Fig. 10). In particular, the driving forces needed for the slide's emergence in Area A were greater than that in Area C. Therefore, the Haya Slide exhibits a lateral variation of frontal emplacement (Fig. 10); i.e. full frontal confinement in Area A, partial confinement across several staircase-like frontal ramps in Area B, to frontal emergence in Area C. Lateral friction along the Northern Lateral Margin may have also locally increased the resisting force in addition to the basal friction (e.g. Joanne et al. 2013), such that the slide is frontally-confined in that area despite being at its thinnest (Fig. 6d).

There is also a broad correlation between the basal shear surface morphology (i.e. depth and slope gradient break) and the overlying structural style in the toe domain. In Area A, for example, a relatively flat gradient, coupled with a deep basal shear surface, is associated with a steep (*c.* 60°) frontal margin (Figs. 4a and 10). This steep frontal margin represents the youngest forethrust that was formed as the slide ceased to translate (Fig. 11a) (e.g. Watt et al. 2012; Joanne et al. 2013; Alsop et al. 2019).

In contrast, Area C displays a low-angle (3°), upslope-dipping, and relatively shallow basal shear surface related to the frontal ramp and slide emergence onto the coeval basin floor (Figs. 4c and 10). Here, a bathymetric high (see Fig. 6a-c) that existed prior to slide emplacement formed inclined strata ahead of the slide. This inclination increased the impact of the slide onto the substrate as also documented in Ogata et al. (2014b). The increased impact led to: (i) the formation of basal shear zone, and (ii) allowed the slide to transfer remaining exerted stress by abandoning the basal shear surface and translate on the coeval seafloor (Fig. 11b). Such distal bathymetric confinement has also been documented elsewhere, for instance, in offshore Colombia, where channel-levee morphology could deflect and/or block debris flows (Ortiz-Karpf et al. 2017).

Areas A and C represent end-member styles of the basal shear surfaces frontal geometry (i.e. frontally-confined and frontally-emergent). Morphologically, the basal shear surface in Area B lies between Areas A and C, being defined by a low-angle (1°) surface, an intermediate-depth and a staircase-like set of frontal ramps (Fig. 4b and 10). The formation of these ramps can be compared to the ramps and flats present along non-planar thrust faults, where the ramps tend to form in relatively high-shear strength layers, and the flats (e.g. basal shear surface connecting the ramps) in weaker layers (Fossen 2016). The potential energy of the slide in Area B might have been progressively (rather than instantaneously) dissipated in the distal area (Fig. 11c). Here, the basal shear surface may have propagated downslope along a horizon until it encountered a layer with higher shear strength (i.e. the red point in Fig. 11c). At that point, the basal shear surface stepped-up through stratigraphy and continued to propagate in shallower levels (i.e. initiated from the green point in Fig. 11c). This process might have continued several times to form the staircase-like frontal ramps, eventually terminating when the shear strength of the strata ahead of the flow exceeded the shear stress exerted by the slide (Fig. 11c). Alternatively, the staircase-like geometry might represent a transitional style between full frontal confinement and full frontal emergence. The first frontal ramp in Area B links along-strike to the frontal ramp in Area A (Fig. 3a). Thus, this first step can be interpreted as the initial toewall. However, this initial toewall was not developed to form a steep ramp such as that in Area A. Instead, the debrite-like seismic facies above the subsequent steps might represent a style of frontal emergence (Fig. 4b). Consequently, the slide must have abandoned the basal shear surface, and progressively shallowed and incorporated material downdip from the initial toewall. This differs to Area C where the slide expelled material on to the coeval basin floor.

There is also some degree of correlation between the depth of the basal shear surface and the degree of disaggregation adjacent to the toewall. In Area A, where the basal shear surface is deeply rooted, internal reflections of the slide are well-preserved (Fig. 11a). In contrast, in Areas B and C, where the basal shear surface progressively shallows, internal reflections of the slide exhibit debritic facies, indicating internal disaggregation (Fig. 11b-c). A similar relationship has also been documented in the thinner part of MTDs in offshore Brazil (Alves & Cartwright 2009; Gamboa et al. 2011) and offshore Colombia (Ortiz-Karpf et al. 2017). These studies conclude that the shallowing basal shear surface led to an increase in shear stress at the base of the flow with increased disaggregation.

Hence, we conclude that the interplay between stresses exerted by parent flow and variation of mechanical properties of the substrate (both locally and regionally), controls the morphology of the basal shear surface (Figs. 10 and 11) (Bull et al. 2009; Shanmugam 2015; Hodgson et al. 2018; Sobiesiak et al. 2018).

Lateral variability of intra-MTD strain

Only a few studies have used seismic reflection data to quantify intra-MTD strain (Bull & Cartwright 2019; Steventon et al. 2019). More specifically, these studies have focused on: (i) strain balancing between headwall and toe domains of MTDs located in offshore Uruguay (Steventon et al. 2019) and offshore Norway (i.e. Confined Stroregga Slide (CSS), Bull & Cartwright 2019); and (ii) assessment of depth-dependant layer shortening in the toe domain (Steventon et al. 2019). The Uruguay example shows that contractional strain in the toe domain is apparently greater than (by *c.* 3-14%), and thus does not balance, extensional strain in the headwall domain (Steventon et al. 2019). This strain deficit could be attributed to sub-seismic penetrative strain, likely associated with grain-scale deformation, and porosity and fluid loss (Koyi 1995; Koyi et al. 2004; Burberry 2015; Dalton et al. 2017; Alsop et al. 2019). In contrast, the study of the CSS found that extensive sediment depletion in the headwall domain is accommodated by only relatively mild contraction (*c.* 5%) in the toe domain (Bull & Cartwright 2019). This discrepancy is inferred to reflect a subsequent phase of deformation that involved the removal of a significant amount of material from the headwall domain after emplacement of the CSS.

Besides longitudinal balancing of MTDs, seismic-scale vertical variability of intra-MTD strain has also been documented. Steventon et al. (2019) documented that the deeper horizon (i.e. closer to the basal shear surface) experienced more shortening (*c.* 27%) than the shallower horizons (*c.* 18%) in the toe domain of the MTD, offshore Uruguay. We find similar results in the Haya Slide, where deeper (H1) and shallower (H2) horizons record *c.* 14% and *c.* 8% of shortening, respectively (Fig. 4a). These observations suggest that the magnitude of shortening estimate depends on the measurement depth due to depth-dependant horizontal shortening, with strain being greatest at depth. Physical models of horizontal shortening suggest that the increase of shortening with depth is balanced by bed-length decrease, lateral compaction of deeper layers, layer-normal thickening of shallower layers, and increased thrust displacement (Koyi 1995; Koyi et al. 2004; Burberry 2015). One or a combination of these processes might occur within the toe domain of a seismic-scale MTD.

The examples above show that intra-MTD strain varies both longitudinally and vertically. Our along-strike analysis of PB-3 and its associated thrusts indicate that intra-MTD strain also varies laterally, with a shear zone separating two domains of contraction within a translated mass (Fig. 8). This represents a seismic-scale example of the field data-derived, multi-cell flow model of Alsop & Marco (2014) (see also Farrell 1984). This model states that a first-order, single-cell MTD is composed of many smaller, second-order flow cells that are formed during translation and may locally interact (Alsop & Marco 2014). This local interaction is revealed by our along-strike analysis of PB-3, which we infer is contained within a more extensive, first-order cell. The eastern and western domains of the pop-up block represent second-order flow cells, with the shear zone representing the flow cells boundary.

In the context of the multi-cell flow model, the formation processes of the structural configurations of PB-3 could be captured in a simplified schematic model comprising three phases of development. In Phase 1, PB-3 might initially have been a single body (or cell) of sediment experiencing the same amount of stress laterally, leading to the formation of a through-going master forethrust (i.e. F-1 in Fig. 12a), i.e. analogous to FT-1 in Figure 8. An alternative interpretation is that the curved fault trace of F-1 in map-view (i.e. similar to FT-1 in Fig. 8a-b) and its slightly bimodal throw profile on strike projection (i.e. similar to FT-1 in Fig. 8c), together suggest that F-1 formed due to a merger of two thrust segments (e.g. Schreurs et al. 2016). Each thrust segment bound the frontal margin of proto

PB-3a and PB-3b, with the linkage point between them now indicated by a local minimum on its throw profile (Fig. 12a).

In Phase 2, velocity perturbations during translation of the first-order cell initiated the formation of the sub-orthogonal shear zone and caused formation of the two second-order flow cells (i.e. the western and eastern cells, Fig. 12b) within the initially continuous cell (i.e. Fig. 12a). The velocity perturbations could be induced by: (i) variable basal shear stress resulting from thickness variation of the first-order cell (i.e. thinning westwards, see Figs. 3a and 12b) (e.g. Alsop & Marco 2014), and/or (ii) early deceleration of the eastern cell as the shear zone became sub-parallel to F-1, associated with the closer position of the eastern cell relative to the frontal confinement of Area A (see Fig. 3b and 12b) (e.g. Steventon et al. 2019).The shear zone laterally partitioned the amount of stress across the PB-3, resulting in differential structural growth in the eastern and western cells forming PB-3a and PB-3b-c, respectively (Fig. 12b).

In Phase 3, downslope translation of the eastern cell ceased prior to the western cell. The still-moving western cell accommodated the still-applied stresses imposed by material towards its rear by the formation of additional contractional structures and the growth of existing structures (i.e. PB-3b and c, Fig. 12c). Hence, the western cell records a more advanced stage of contraction than the eastern cell, as expressed by the higher number of thrusts and the larger cumulative throw of the thrusts (Fig. 12c) (e.g. Cartwright et al. 1995; Totake et al. 2018). This process results in an along-strike variability in the style and magnitude of intra-MTD strain, with the shear zone separating the intra-MTD cells that record the different amount of strain.

Impact of intra-MTD strain on seal potential

MTDs can play at least two roles in the development of petroleum systems: they commonly serve as seals (Algar et al. 2011; Cardona et al. 2016), and more rarely act as reservoirs (Sawyer et al. 2007; Algar et al. 2011; Shanmugam 2012; Arfai et al. 2016; Cardona et al. 2016). This is controlled by three key parameters: (i) provenance lithology, most notably sand/mud ratio (Jenner et al. 2007; Omosanya

& Alves 2013), (ii) substrate lithology and erodibility (e.g. Cardona et al. 2020), and (iii) the degree of internal disaggregation, where a strongly disaggregated MTD could have high seal potential due to significant permeability reduction (Alves et al. 2014; Omeru 2014; Cardona et al. 2016). The driving factors of this permeability reduction include: (i) internal lithological mixing of fine and coarse grains that produces an unsorted matrix (Ogata et al. 2019); (ii) alignment of clay minerals due to shearing during transport (Bennett et al. 1991; Ikari & Saffer 2012; Cardona et al. 2016); and (iii) grain crushing in otherwise good-quality reservoirs (Crawford 1998).

The seal potential of highly-disaggregated cohesive MTDs may be compromised by two factors. First, the entrainment of coarser-grained substrate, such as by a debris flow that overrides earlier sandy turbidites, could result in sandier, and less cohesive debrite downslope (Dykstra et al. 2011; Ortiz-Karpf et al. 2017). This incorporation of sandy materials could also lead to an increase of pore-scale (μm) effective porosity and permeability (Dykstra et al. 2011). Second, large (km-scale) rafted blocks (megaclasts) with reservoir potential, encased within an otherwise very fine-grained, low-permeability debritic matrix of an MTD (Gamboa & Alves 2015; Cardona et al. 2016; Cardona et al. 2020), could provide localised high-permeability zones (e.g. internal faults and fractures) that can promote fluid migration and hydrocarbon leakage (Gamboa & Alves 2015). The pore-scale permeability variations can only be inferred from well logs (e.g. Sun & Alves 2020), cores (e.g. Tripsanas et al. 2003), and outcrops (Dykstra et al. 2011; Ogata et al. 2019). However, only 3D seismic reflection data allow three-dimensional analysis of the megaclast-scale, high-permeability zones (Gamboa & Alves 2015; Cox et al. 2020). Therefore, integration of multi-scale data types is essential (e.g. Dykstra et al. 2011; Ogata et al. 2014a), where possible, thereby enabling comprehensive analysis of the seal potential of MTDs (e.g. Cardona et al. 2016).

Seal competence can vary longitudinally, from head to toe domains of the MTD, due to substrate entrainment and shearing during transport (e.g. Cardona et al. 2020). The Haya Slide is a clay-rich MTD that contains debritic facies in the inner part; this area may therefore represent a good hydrocarbon seal when compared to the imbricated, but otherwise internally moderately undeformed blocks present in the outer part (Figs. 3b and 4).

In the outer part, however, we also document notable along-strike variations in seismic facies (Fig. 4). For instance, Area A is characterised by imbricated thrusts. If these thrusts lack clay smear and are relatively permeable compared to the flanking, very fine-grained host rock, they may be conduits for fluid migration, implying a higher seal risk for this area (i.e. low seal potential). Towards Area C, seismic facies become more chaotic and transparent, suggesting a higher degree of deformation and internal disaggregation. Seismic facies in Area C may thus suggest a better seal potential here than in Area A because chaotic and transparent seismic facies have higher seal potential than blocky MTDs containing preserved stratigraphy (Alves et al. 2014; Omeru 2014). Therefore, our results suggest that seal potential of an MTD can vary along both depositional dip and strike within any one domain.

CONCLUSIONS

A recent mass-transport complex (MTD), the Haya Slide, has been characterised in the Makassar Strait based on high-quality 3D seismic reflection and bathymetry data. The slide originated from the collapsed flank of an anticline in the NE and transported radially to the SW. An along-strike analysis of the toe domain of the slide has provided the following conclusions:

1. The inner part of the toe domain is characterised by a debrite, which passes, first, downdip into megaclast-bearing debrite and, second, into coherent pop-up blocks towards the outer part. The debrite and the pop-up blocks are genetically-related, bound by the same surfaces (i.e. basal shear surface and seabed). Lateral loading by the debrite onto coherent strata induced progressive downslope failure. Shortening estimates across the coherent strata show 8-14% of shortening, equating to 0.6-1.1 km of downslope translation.
2. The outer part of the toe domain exhibits the variations in: (i) depth and gradient of the basal shear surface, (ii) trend and spacing of the pop-up blocks and their associated thrust faults, and (iii) frontal geometry. A deep and relatively flat basal shear surface is associated with

frontal confinement, where steep ramp separates undeformed strata and the slide. A shallow and upflow-dipping basal shear surface is associated with frontal emergence of the slide onto the coeval basin floor. Between these two extremes, the frontal geometry is characterised by staircase-like frontal ramps. Internal architecture of the slide may also be related to the geometry of the basal shear surface, where highly disaggregated material can be associated with the progressive downslope-shallowing basal shear surface. The interplay between drop height (i.e. driving force), and along-strike depth variation of basal shear surface (i.e. resistive force), likely to determine the lateral variability of frontal geometry of the slide. For instance, where resistive force < driving force led to frontal emergence, otherwise the slide would be frontally confined.

3. A detailed study of fold-and-thrust structures within the region of pop-up block shows along-strike variability of intra-MTD strain. This shows western and eastern regions of the toe domain, separated by a sub-orthogonal shear zone, experiencing different amounts of contraction. The western regime records a higher amount of strain, reflecting a more advanced phase of structural growth, i.e. indicated by higher throw values and number of thrusts, compared to its eastern counterpart.

4. MTDs commonly serve as seals in a petroleum system. However, previous studies have shown that MTDs could have variable seal potential based on its axial domains (headwall to toe) due to different degree of disaggregation and substrate entrainment. MTDs that are dominated by mud-rich debrite are likely to have good seal potential because the combination of low-permeability matrix and clay mineral alignment reduces pore throat size and connectivity. In contrast, MTDs that contain blocky facies with imbricated thrusts, could have lower seal potential because larger pore-throat properties (if they are sand-rich), and open fracture systems (e.g. thrusts that lack clay smear and are relatively more permeable than the surrounding host rock) could aid fluid flow. The Haya Slide shows that the debritic and blocky facies of an MTD could co-exist longitudinally (e.g. debrite in the headwall-to-translational

domains and fold-and-thrust systems in the toe domain). More importantly, the slide also exhibits lateral variations of the internal facies (e.g. fold-and-thrust systems could laterally pass to debrite within the toe domain). Therefore, these longitudinal and lateral variations of facies, and associated rock properties, should be considered when assessing MTD seal potential in petroleum systems.

ACKNOWLEDGEMENT

We thank Information and Data Centre, Ministry of Energy and Mineral Resources (PUSDATIN ESDM) of the Republic of Indonesia for providing 3D seismic reflection and well data, and TGS for providing multibeam bathymetry and near-seabed core data. Schlumberger, Geoteric and Midland Valley Exploration for granting software licences to Imperial College London. The first author thanks the Indonesia Endowment Fund for Education (LPDP) (Grant No.: 20160822019161) for its financial support. We thank the editor, Giovanni Camanni, and the reviewers, Kei Ogata and an anonymous reviewer, for constructive reviews that significantly improve the earlier version of this manuscript. Thank you also to Michael Steventon and Sophie Pan for discussions on structural interpretation techniques.

CONFLICT OF INTEREST

No conflict of interest declared.

REFERENCES

Algar, S., Milton, C., Upshall, H., Roestenburg, J. & Crevello, P. 2011. Mass-transport deposits of the deepwater northwestern Borneo margin - Characterization from seismic-reflection, borehole, and core data with implications for hydrocarbon exploration and exploitation. *Mass-transport deposits in deepwater settings: Society for Sedimentary Geology (SEPM) Special Publication 96*, 7-38.

Allen, G.P. & Chambers, J.L. 1998. *Sedimentation in the modern and Miocene Mahakam Delta*. Indonesian Petroleum Association, Jakarta.

Alsop, G.I. & Marco, S. 2014. Fold and fabric relationships in temporally and spatially evolving slump systems: A multi-cell flow model. *Journal of Structural Geology*, **63**, 27-49.

Alsop, G.I., Weinberger, R., Marco, S. & Levi, T. 2019. Fold and Thrust Systems in Mass-Transport Deposits Around the Dead Sea Basin. *Submarine Landslides: Subaqueous Mass Transport Deposits from Outcrops to Seismic Profiles*, 139-153.

Alves, T.M. 2015. Submarine slide blocks and associated soft-sediment deformation in deep-water basins: A review. *Marine and Petroleum Geology*, **67**, 262-285.

Alves, T.M. & Cartwright, J.A. 2009. Volume balance of a submarine landslide in the Espírito Santo Basin, offshore Brazil: Quantifying seafloor erosion, sediment accumulation and depletion. *Earth and Planetary Science Letters*, **288**, 572-580, http://doi.org/10.1016/j.epsl.2009.10.020.

Alves, T.M., Kurtev, K., Moore, G.F. & Strasser, M. 2014. Assessing the internal character, reservoir potential, and seal competence of mass-transport deposits using seismic texture: A geophysical and petrophysical approach. *AAPG Bulletin*, **98**, 793-824, http://doi.org/10.1306/09121313117.

Arfai, J., Lutz, R., Franke, D., Gaedicke, C. & Kley, J. 2016. Mass-transport deposits and reservoir quality of Upper Cretaceous Chalk within the German Central Graben, North Sea. *International Journal of Earth Sciences*, **105**, 797-818.

Armandita, C., Morley, C.K. & Rowell, P. 2015. Origin, structural geometry, and development of a giant coherent slide: The South Makassar Strait mass transport complex. *Geosphere*, **11**, 376-403, http://doi.org/10.1130/ges01077.1.

Bennett, R.H., Bryant, W.R. & Hulbert, M.H. 1991. *Microstructure of fine-grained sediments: From mud to shale*. Springer Science & Business Media.

Brackenridge, R., Nicholson, U., Sapiie, B., Stow, D. & Tappin, D. 2020. Indonesian Throughflow as a preconditioning mechanism for submarine landslides in the Makassar Strait. *Geological Society, London, Special Publications*, **500**.

Bull, S. & Cartwright, J.A. 2019. Line length balancing to evaluate multi-phase submarine landslide development: an example from the Storegga Slide, Norway. *Geological Society, London, Special Publications*, **500**.

Bull, S., Cartwright, J. & Huuse, M. 2009. A review of kinematic indicators from mass-transport complexes using 3D seismic data. *Marine and Petroleum Geology*, **26**, 1132-1151, http://doi.org/10.1016/j.marpetgeo.2008.09.011.

Burberry, C.M. 2015. Spatial and temporal variation in penetrative strain during compression: Insights from analog models. *Lithosphere*, **7**, 611-624.

Butler, R. & McCaffrey, W. 2010. Structural evolution and sediment entrainment in mass-transport complexes: outcrop studies from Italy. *Journal of the Geological Society*, **167**, 617-631.

Cardona, S., Wood, L.J., Day-Stirrat, R.J. & Moscardelli, L. 2016. Fabric development and pore-throat reduction in a mass-transport deposit in the Jubilee Gas Field, Eastern Gulf of Mexico: consequences for the sealing capacity of MTDs *Submarine Mass Movements and their Consequences*. Springer, 27-37.

Cardona, S., Wood, L.J., Dugan, B., Jobe, Z. & Strachan, L.J. 2020. Characterization of the Rapanui mass-transport deposit and the basal shear zone: Mount Messenger Formation, Taranaki Basin, New Zealand. *Sedimentology*, http://doi.org/10.1111/sed.12697.

Cartwright, J.A., Trudgill, B.D. & Mansfield, C.S. 1995. Fault growth by segment linkage: an explanation for scatter in maximum displacement and trace length data from the Canyonlands Grabens of SE Utah. *Journal of Structural Geology*, **17**, 1319-1326.

Chopra, S. & Marfurt, K.J. 2007. *Seismic attributes for prospect identification and reservoir characterization*. Society of Exploration Geophysicists Tulsa, Oklahoma.

Clare, M., Chaytor, J., Dabson, O., Gamboa, D., Georgiopoulou, A., Eady, H., Hunt, J., Jackson, C., *et al.* 2018. A consistent global approach for the morphometric characterization of subaqueous landslides. *Geological Society, London, Special Publications*, **477**, SP477. 415.

Cloke, I., Milsom, J. & Blundell, D. 1999. Implications of gravity data from East Kalimantan and the Makassar Straits: a solution to the origin of the Makassar Straits? *Journal of Asian Earth Sciences*, **17**, 61-78.

Cox, D.R., Huuse, M., Newton, A.M., Gannon, P. & Clayburn, J. 2020. Slip sliding away: Enigma of large sandy blocks within a gas-bearing mass transport deposit, offshore northwestern Greenland. *AAPG Bulletin*, **104**, 1011-1043.

Crawford, B. 1998. Experimental fault sealing: shear band permeability dependency on cataclastic fault gouge characteristics. *Geological Society, London, Special Publications*, **127**, 27-47.

Dahlstrom, C. 1969. Balanced cross sections. *Canadian Journal of Earth Sciences*, **6**, 743-757.

Dalton, T., Paton, D., Oldfield, S., Needham, D. & Wood, A. 2017. The importance of missing strain in Deep Water Fold and Thrust Belts. *Marine and Petroleum Geology*, **82**, 163-177.

Daly, M., Cooper, M., Wilson, I., Smith, D.t. & Hooper, B. 1991. Cenozoic plate tectonics and basin evolution in Indonesia. *Marine and Petroleum Geology*, **8**, 2-21.

Dott, R. 1963. Dynamics of subaqueous gravity depositional processes. *AAPG Bulletin*, **47**, 104-128.

Dykstra, M., Garyfalou, K., Kertznus, V., Kneller, B., Milana, J.P., Molinaro, M., Szuman, M. & Thompson, P. 2011. Mass-transport deposits: Combining outcrop studies and seismic forward modeling to understand lithofacies distributions, deformations, and their seismic stratigraphic expression. *SEPM Special Publication*, **96**, 293-310.

Eckersley, A.J., Lowell, J. & Szafian, P. 2018. High-definition frequency decomposition. *Geophysical Prospecting*, **66**, 1138-1143.

Ellis, M.A. & Dunlap, W.J. 1988. Displacement variation along thrust faults: Implications for the development of large faults. *Journal of Structural Geology*, **10**, 183-192.

Farrell, S.G. 1984. A dislocation model applied to slump structures, Ainsa Basin, South Central Pyrenees. *Journal of Structural Geology*, **6**, 727-736.

Festa, A., Ogata, K., Pini, G.A., Dilek, Y. & Alonso, J.L. 2016. Origin and significance of olistostromes in the evolution of orogenic belts: A global synthesis. *Gondwana Research*, **39**, 180-203.

Fossen, H. 2016. *Structural geology*. Cambridge University Press.

Frey-Martinez, J., Cartwright, J. & Hall, B. 2005. 3D seismic interpretation of slump complexes: examples from the continental margin of Israel. *Basin Research*, **17**, 83-108, http://doi.org/10.1111/j.1365-2117.2005.00255.x.

Frey-Martínez, J., Cartwright, J. & James, D. 2006. Frontally confined versus frontally emergent submarine landslides: A 3D seismic characterisation. *Marine and Petroleum Geology*, **23**, 585-604, http://doi.org/10.1016/j.marpetgeo.2006.04.002.

Gamboa, D. & Alves, T.M. 2015. Three-dimensional fault meshes and multi-layer shear in mass-transport blocks: Implications for fluid flow on continental margins. *Tectonophysics*, **647**, 21-32.

Gamboa, D., Alves, T. & Cartwright, J. 2011. Distribution and characterization of failed (mega) blocks along salt ridges, southeast Brazil: Implications for vertical fluid flow on continental margins. *Journal of Geophysical Research: Solid Earth*, **116**.

Gee, M., Gawthorpe, R. & Friedmann, J. 2005. Giant striations at the base of a submarine landslide. *Marine Geology*, **214**, 287-294.

Gee, M., Uy, H., Warren, J., Morley, C. & Lambiase, J. 2007. The Brunei slide: a giant submarine landslide on the North West Borneo Margin revealed by 3D seismic data. *Marine Geology*, **246**, 9-23.

Gee, M.J., Masson, D.G., Watts, A.B. & Mitchell, N.C. 2001. Passage of debris flows and turbidity currents through a topographic constriction: seafloor erosion and deflection of flow pathways. *Sedimentology*, **48**, 1389-1409.

Guntoro, A. 1999. The formation of the Makassar Strait and the separation between SE Kalimantan and SW Sulawesi. *Journal of Asian Earth Sciences*, **17**, 79-98.

Higgins, S., Clarke, B., Davies, R.J. & Cartwright, J. 2009. Internal geometry and growth history of a thrust-related anticline in a deep water fold belt. *Journal of Structural Geology*, **31**, 1597-1611.

Hodgson, D., Brooks, H., Ortiz-Karpf, A., Spychala, Y., Lee, D. & Jackson, C.-L. 2018. Entrainment and abrasion of megaclasts during submarine landsliding and their impact on flow behaviour. *Geological Society, London, Special Publications*, **477**, SP477. 426.

Huiqi, L., McClay, K. & Powell, D. 1992. Physical models of thrust wedges *Thrust tectonics*. Springer, 71-81.

Huvenne, V.A., Croker, P.F. & Henriet, J.P. 2002. A refreshing 3D view of an ancient sediment collapse and slope failure. *Terra Nova*, **14**, 33-40.

Ikari, M.J. & Saffer, D.M. 2012. Permeability contrasts between sheared and normally consolidated sediments in the Nankai accretionary prism. *Marine Geology*, **295**, 1-13.

Jackson, C.A. 2011. Three-dimensional seismic analysis of megaclast deformation within a mass transport deposit; implications for debris flow kinematics. *Geology*, **39**, 203-206.

Jenner, K.A., Piper, D.J., Campbell, D.C. & Mosher, D.C. 2007. Lithofacies and origin of late Quaternary mass transport deposits in submarine canyons, central Scotian Slope, Canada. *Sedimentology*, **54**, 19-38.

Joanne, C., Lamarche, G. & Collot, J.Y. 2013. Dynamics of giant mass transport in deep submarine environments: the Matakaoa Debris Flow, New Zealand. *Basin Research*, **25**, 471-488.

Koyi, H. 1995. Mode of internal deformation in sand wedges. *Journal of Structural Geology*, **17**, 293-300.

Koyi, H.A., Sans, M., Teixell, A., Cotton, J. & Zeyen, H. 2004. The significance of penetrative strain in the restoration of shortened layers—Insights from sand models and the Spanish Pyrenees. *In*: McClay, K.R. (ed) *Thrust tectonics and hydrocarbon systems*. AAPG Memoir, **82**, p. 207-222.

Lastras, G., Canals, M., Urgeles, R., Hughes-Clarke, J.E. & Acosta, J. 2004. Shallow slides and pockmark swarms in the Eivissa Channel, western Mediterranean Sea. *Sedimentology*, **51**, 837-850.

Liu, S. & Dixon, J.M. 1995. Localization of duplex thrust-ramps by buckling: analog and numerical modelling. *Journal of Structural Geology*, **17**, 875-886.

Mandl, G. & Crans, W. 1981. Gravitational gliding in deltas. *Geological Society, London, Special Publications*, **9**, 41-54.

Martinsen, O. & Bakken, B. 1990. Extensional and compressional zones in slumps and slides in the Namurian of County Clare, Ireland. *Journal of the Geological Society*, **147**, 153-164.

Masson, D., Huggett, Q. & Brunsden, D. 1993. The surface texture of the Saharan debris flow deposit and some speculations on submarine debris flow processes. *Sedimentology*, **40**, 583-598.

Mayer, B. & Damm, P. 2012. The Makassar Strait throughflow and its jet. *Journal of Geophysical Research: Oceans*, **117**.

Moernaut, J. & De Batist, M. 2011. Frontal emplacement and mobility of sublacustrine landslides: results from morphometric and seismostratigraphic analysis. *Marine Geology*, **285**, 29-45.

Moore, G.F., Saffer, D., Studer, M. & Pisani, P.C. 2011. Structural restoration of thrusts at the toe of the Nankai Trough accretionary prism off Shikoku Island, Japan: Implications for dewatering processes. *Geochemistry, Geophysics, Geosystems*, **12**.

Moscardelli, L. & Wood, L. 2008. New classification system for mass transport complexes in offshore Trinidad. *Basin Research*, **20**, 73-98, http://doi.org/10.1111/j.1365-2117.2007.00340.x.

Nardin, T.R., Hein, F., Gorsline, D.S. & Edwards, B. 1979. A review of mass movement processes sediment and acoustic characteristics, and contrasts in slope and base-of-slope systems versus canyon-fan-basin floor systems. *In*: Doyle, L.E. & Pilkey, O.H. (eds) *Geology of continental slopes*. Soc. Econ. Paleont. and Min. Special Publication 27, 61-74.

Nemec, W. 1991. Aspects of sediment movement on steep delta slopes. *In*: Colella, A. & Prior, D.B. (eds) *Coarsed-Grained Deltas*. International Association of Sedimentologists, **10**, 29-73.

Ogata, K., Mutti, E., Pini, G.A. & Tinterri, R. 2012. Mass transport-related stratal disruption within sedimentary mélanges: examples from the northern Apennines (Italy) and south-central Pyrenees (Spain). *Tectonophysics*, **568**, 185-199.

Ogata, K., Mountjoy, J., Pini, G.A., Festa, A. & Tinterri, R. 2014a. Shear zone liquefaction in mass transport deposit emplacement: a multi-scale integration of seismic reflection and outcrop data. *Marine Geology*, **356**, 50-64.

Ogata, K., Festa, A., Pini, G., Pogačnik, Ž. & Lucente, C. 2019. Substrate deformation and incorporation in sedimentary mélanges (olistostromes): Examples from the northern Apennines (Italy) and northwestern Dinarides (Slovenia). *Gondwana Research*, **74**, 101-125.

Ogata, K., Pogačnik, Ž., Pini, G.A., Tunis, G., Festa, A., Camerlenghi, A. & Rebesco, M. 2014b. The carbonate mass transport deposits of the Paleogene Friuli Basin (Italy/Slovenia): internal anatomy and inferred genetic processes. *Marine Geology*, **356**, 88-110.

Omeru, T. 2014. *Mass Transport Deposits: Implications for Reservoir Seals*. (PhD Thesis) Cardiff University, Cardiff

Omeru, T. & Cartwright, J.A. 2019. The efficacy of kinematic indicators in a complexly deformed Mass Transport Deposit: Insights from the deepwater Taranaki Basin, New Zealand. *Marine and Petroleum Geology*, **106**, 74-87.

Omosanya, K.O. & Alves, T.M. 2013. A 3-dimensional seismic method to assess the provenance of Mass-Transport Deposits (MTDs) on salt-rich continental slopes (Espírito Santo Basin, SE Brazil). *Marine and Petroleum Geology*, **44**, 223-239.

Ortiz-Karpf, A., Hodgson, D.M., Jackson, C.A.-L. & McCaffrey, W.D. 2017. Influence of Seabed Morphology and Substrate Composition On Mass-Transport Flow Processes and Pathways: Insights From the Magdalena Fan, Offshore Colombia. *Journal of Sedimentary Research*, **87**, 189-209.

Partyka, G., Gridley, J. & Lopez, J. 1999. Interpretational applications of spectral decomposition in reservoir characterization. *The Leading Edge*, **18**, 353-360.

Piper, D.J.W., Pirmez, C., Manley, P.L., Long, D., Flood, R.D., Normark, W.R. & Showers, W. 1997. Mass Transport Deposits of the Amazon Fan. *In*: Flood, R.D., Piper, D.J.W., Klaus, A. & Peterson, L.C. (eds.) *Ocean Drilling Program, Scientific Results*, 109-146.

Posamentier, H.W. & Kolla, V. 2003. Seismic geomorphology and stratigraphy of depositional elements in deep-water settings. *Journal of Sedimentary Research*, **73**, 367-388.

Posamentier, H.W. & Martinsen, O.J. 2011. The character and genesis of submarine mass-transport deposits: insights from outcrop and 3D seismic data. *Mass-transport deposits in deepwater settings: Society for Sedimentary Geology (SEPM) Special Publication 96*, 7-38.

Puspita, S.D., Hall, R. & Elders, C.F. 2005. Structural styles of the offshore West Sulawesi fold belt, North Makassar Straits, Indonesia. *Thirtieth IPA Annual Convention & Exhibition*. Indonesian Petroleum Association (IPA), Jakarta.

Roberts, H.H. & Sydow, J. 2003. Late Quaternary stratigraphy and sedimentology of the offshore Mahakam delta, east Kalimantan (Indonesia). *SEPM Special Publication*, **76**, 125-145.

Sanderson, D.J. & Marchini, W. 1984. Transpression. *Journal of Structural Geology*, **6**, 449-458.

Sawyer, D.E., Flemings, P.B., Shipp, R.C. & Winker, C.D. 2007. Seismic geomorphology, lithology, and evolution of the late Pleistocene Mars-Ursa turbidite region, Mississippi Canyon area, northern Gulf of Mexico. *AAPG Bulletin*, **91**, 215-234.

Schnellmann, M., Anselmetti, F.S., Giardini, D. & McKENZIE, J.A. 2005. Mass movement-induced fold-and-thrust belt structures in unconsolidated sediments in Lake Lucerne (Switzerland). *Sedimentology*, **52**, 271-289.

Schreurs, G., Buiter, S.J., Boutelier, J., Burberry, C., Callot, J.-P., Cavozzi, C., Cerca, M., Chen, J.-H.*, et al.* 2016. Benchmarking analogue models of brittle thrust wedges. *Journal of Structural Geology*, **92**, 116-139.

Shanmugam, G. 2012. Origin and Classification of Sandy Mass-Transport Deposits *Handbook of Petroleum Exploration and Production*. Elsevier, **9**, 41-65.

Shanmugam, G. 2015. The landslide problem. *Journal of Palaeogeography*, **4**, 109-166.

Sobiesiak, M.S., Kneller, B., Alsop, G.I. & Milana, J.P. 2016. Internal deformation and kinematic indicators within a tripartite mass transport deposit, NW Argentina. *Sedimentary Geology*, http://doi.org/10.1016/j.sedgeo.2016.04.006.

Sobiesiak, M.S., Kneller, B., Alsop, G.I. & Milana, J.P. 2018. Styles of basal interaction beneath mass transport deposits. *Marine and Petroleum Geology*, **98**, 629-639.

Sobiesiak, M.S., Buso, V.V., Kneller, B., Alsop, G.I. & Milana, J.P. 2019. Block Generation, Deformation, and Interaction of Mass-Transport Deposits With the Seafloor: An Outcrop-Based Study of the Carboniferous Paganzo Basin (Cerro Bola, NW Argentina). *Submarine Landslides: Subaqueous Mass Transport Deposits from Outcrops to Seismic Profiles*, 91-104.

Steventon, M.J., Jackson, C.A., Hodgson, D.M. & Johnson, H.D. 2019. Strain analysis of a seismically imaged mass-transport complex, offshore Uruguay. *Basin Research*, **31**, 600-620.

Strachan, L.J. 2002. *Geometry to genesis: a comparative field study of slump deposits and their modes of formation.* University of Wales. Cardiff.

Sun, Q. & Alves, T. 2020. Petrophysics of fine-grained mass-transport deposits: A critical review. *Journal of Asian Earth Sciences*, **192**, 104291, https://doi.org/10.1016/j.jseaes.2020.104291.

Takagi, H., Pratama, M.B., Kurobe, S., Esteban, M., Aránguiz, R. & Ke, B. 2019. Analysis of generation and arrival time of landslide tsunami to Palu City due to the 2018 Sulawesi earthquake. *Landslides*, **16**, 983-991.

Tappin, D., Watts, P., McMurtry, G., Lafoy, Y. & Matsumoto, T. 2001. The Sissano, Papua New Guinea tsunami of July 1998—offshore evidence on the source mechanism. *Marine Geology*, **175**, 1-23.

Totake, Y., Butler, R.W., Bond, C.E. & Aziz, A. 2018. Analyzing structural variations along strike in a deep-water thrust belt. *Journal of Structural Geology*, **108**, 213-229.

Trincardi, F. & Argnani, A. 1990. Gela submarine slide: a major basin-wide event in the Plio-Quaternary foredeep of Sicily. *Geo-Marine Letters*, **10**, 13.

Tripsanas, E., Bryant, W. & Prior, D. 2003. Structural characteristics of cohesive gravity-flow deposits, and a sedimentological approach on their flow mechanisms *Submarine Mass Movements and Their Consequences*. Springer, 129-136.

Van Der Merwe, W.C., Hodgson, D.M. & Flint, S.S. 2011. Origin and terminal architecture of a submarine slide: a case study from the Permian Vischkuil Formation, Karoo Basin, South Africa. *Sedimentology*, **58**, 2012-2038, http://doi.org/10.1111/j.1365-3091.2011.01249.x.

Vanneste, M., Forsberg, C.F., Glimsdal, S., Harbitz, C.B., Issler, D., Kvalstad, T.J., Løvholt, F. & Nadim, F. 2013. Submarine landslides and their consequences: what do we know, what can we do? *Landslide science and practice*. Springer, 5-17.

Walsh, J.J. & Watterson, J. 1991. Geometric and kinematic coherence and scale effects in normal fault systems. *Geological Society, London, Special Publications*, **56**, 193-203.

Watt, S., Talling, P., Vardy, M., Masson, D., Henstock, T., Hühnerbach, V., Minshull, T., Urlaub, M.*, et al.* 2012. Widespread and progressive seafloor-sediment failure following volcanic debris avalanche emplacement: Landslide dynamics and timing offshore Montserrat, Lesser Antilles. *Marine Geology*, **323**, 69-94.

Weimer, P. & Shipp, C. 2004. Mass Transport Complexes: Musing on past uses and suggestions for future directions. *Offshore Technology Conference*, Houston.

Zeng, H., Henry, S.C. & Riola, J.P. 1998. Stratal slicing, Part II: Real 3-D seismic data. *Geophysics*, **63**, 514-522.

FIGURE CAPTIONS

Fig. 1. Geological setting and location map of the study area. **(a)** The Makassar Strait is surrounded by tectonically active regions, where Eurasia, Indo-Australia, Philippine Sea and Pacific plates interact. A strong ocean current flowing from Pacific towards Indian oceans, Indonesia Throughflow (ITF), flows through the Makassar Strait (red arrow). **(b)** The study area is located in the southern end of Labani Channel, that connects the North and South Makassar basins. Major structural features include fault zones (Palu-Koro and Paternoster fault zones) and fold-thrust belts (e.g. Brackenridge et al., 2020; Cloke et al., 1999). The fold-thrust belts are divided into the Northern (NSP), Central (CSP) and Southern (SSP) structural provinces (Puspita et al., 2005). The dark blue line marks the extent of 3D seismic reflection data, and the green line outlines the area covered by multibeam data. Two green dots represent wells within the seismic reflection data. The small, yellow area marks the extent of the Haya Slide (see Fig. 2). Blue and red dots are the location of near-seabed sediment cores of TGS009 and TGS194, respectively. **(c)** A cartoon cross-section across the Makassar Strait showing MTDs accumulation in the basin and their related sources, i.e. prograding shelf (related to Mahakam Delta) in the W and collapse of anticline flanks in the E. Inferred based on Puspita et al. (2005) and Brackenridge et al. (2020). **(d)** A seismic line correlating the Haya Slide (yellow-shaded) and the two wells (i.e. XS-1 and XR-1).

Fig. 2. Seabed topography, as defined by this bathymetry map, shows the external geometry of the Haya Slide. The slide originated from the NE (collapse of the southern flank of a thrust-cored anticline) and transported towards the SW. This study focuses on the toe domain of the slide (red outline), which is mostly imaged by the 3D seismic reflection data (blue outline). The toe domain of the slide has a radial geometry, where the Eastern and Northern lateral margins trending N-S and E-W, respectively.

Fig. 3. Key maps of the Haya Slide. **(a)** Thickness map covering the toe domain of the Haya Slide. The slide is thickest (200 m) in the southern part and thins toward the Northern Lateral Margin. Laterally, three areas can be defined based on its frontal geometry (i.e. Area A, B, and C). An inset map showing the focus area of the slide, captured by 3D seismic reflection data. **(b)** Spectral decomposition map showing internal seismic facies of the slide. Axially, the slide can be divided into inner and outer parts with 'soft' boundary between them. The inner part is dominated by debrite containing megaclasts, and the outer part is dominated by pop-up blocks.

Fig. 4. Seismic sections across Area A, B, and C, showing similar general characteristics, where debrite dominates the inner part, and pop-up blocks dominate the outer part. However, the three areas have different characteristics of frontal margin. **(a)** Area A is characterised by frontal confinement and coherent pop-up blocks. Translation distance was estimated by calculating shortening amount at H1

and 2, i.e. 8-14% shortening equating to 0.6-1.1 km. **(b)** Area B is characterised by frontal ramps with more chaotic reflections adjacent to frontal margin, and less coherent pop-up blocks. **(c)** Area C is characterised by frontal emergence and a broad bulge on the seabed above steeply-inclined detachment surface.

Fig. 5. Deformation ahead of the parent flow. **(a)** Variance time-slice showing distributed shear zone downdip from an intact block. Thrusts forming this distributed shear zone laterally propagate eastwards. **(b)** Seismic section showing distributed shear zone, showing deformed strata ahead immediately downdip from the intact block. Folded strata ahead of the BSS, interpreted as an unformed thrust.

Fig. 6. Relationship between basal shear surface morphology, and seabed in Area C and the adjacent area. **(a)** Basal shear surface structure map showing slope gradient break in Area C. **(b)** Seabed structure map showing a broad area of high seabed relief (seabed bulge). **(c)** Spatial relationship between slope gradient break on the BSS and the occurrence of the seabed bulge, leading to frontal emergence of the slide. **(d)** Seismic section adjacent to Northern Lateral Margin showing closely-spaced pop-up blocks and frontal confinement of the slide.

Fig. 7. The boundary between Areas B and C. **(a)** Variance along the BSS (50 ms windowed above) showing an abrupt boundary between Area B and C. **(b)** A ramp marks the boundary between Area B and C, and expressed as positive relief on the seabed.

Fig. 8. Along-strike quantitative analysis of Pop-up Block 3 (see Fig. 4a). **(a)** Time structure map of H2 (see Fig. 4a) and associated faults. **(b)** Variance time-slice showing lateral extent of Pop-up Block 3. **(c)** Throw vs. Distance (T-x) plot of fore- and backthrusts bounding Pop-up Block 3. Shear zone separates two bodies that have different amount of strain, i.e. the area to the west of the shear zone experienced more contraction as shown by cumulative throw as compared the area eastwards from the shear zone. **(d-f)** Seismic sections showing along-strike variability of faults bounding Pop-up Block 3.

Fig. 9. Schematic model of emplacement processes of the Haya Slide. **(a)** Debris flow, originated from failed anticline (see Fig. 2) entered the basin, deformed the seabed, and then entrained substrate into the flow. **(b)** Substrate erosion and entrainment continued to occur up to the point where the debris flow did not have sufficient shear stress for substrate entrainment. Thus, the remaining exerted stress deformed substrate ahead of the flow (i.e. lateral loading). **(c)** Subsequent compressional deformation occurred, allowing a relatively short translation distance (0.61 to 1.06 km) in the toe domain, which has different frontal geometries along strike.

Fig. 10. A summary of downdip and along-strike variations in Areas A, B and C of the Haya Slide. Note the lateral changes in structural style and internal facies characteristics.

Fig. 11. Evolution of basal shear surface adjacent to the toewall of the Haya Slide, showing development of **(a)** frontal confinement in Area A, **(b)** frontal emergence in Area C, and **(c)** staircase-like frontal ramps in Area B, which is an intermediate (transitional) style between frontal confinement and emergence.

Fig. 12. A simplified schematic depiction of along-strike strain variability within PB-3 (see Figs. 3b, 4a and 8). **(a)** An initial stage of PB-3 formation, where it experienced similar amount of stress along strike forming a through-going, master forethrust (F-1). **(b)** Intra-MTD velocity perturbations led to the formation of a curved, sub-orthogonal shear zone, resulting in the formation of second-order flow cells (i.e. eastern and western cells), and along-strike stress partitioning by the shear zone led to the formation of PB-3a-c. **(c)** The eastern cell halted earlier than the western cell due to closer frontal confinement (i.e. Area A), so that the still-translating western cell experienced more strain as indicated by the higher number of thrusts and cumulative throw values. Inspired by Totake et al. (2018).

Figure 1

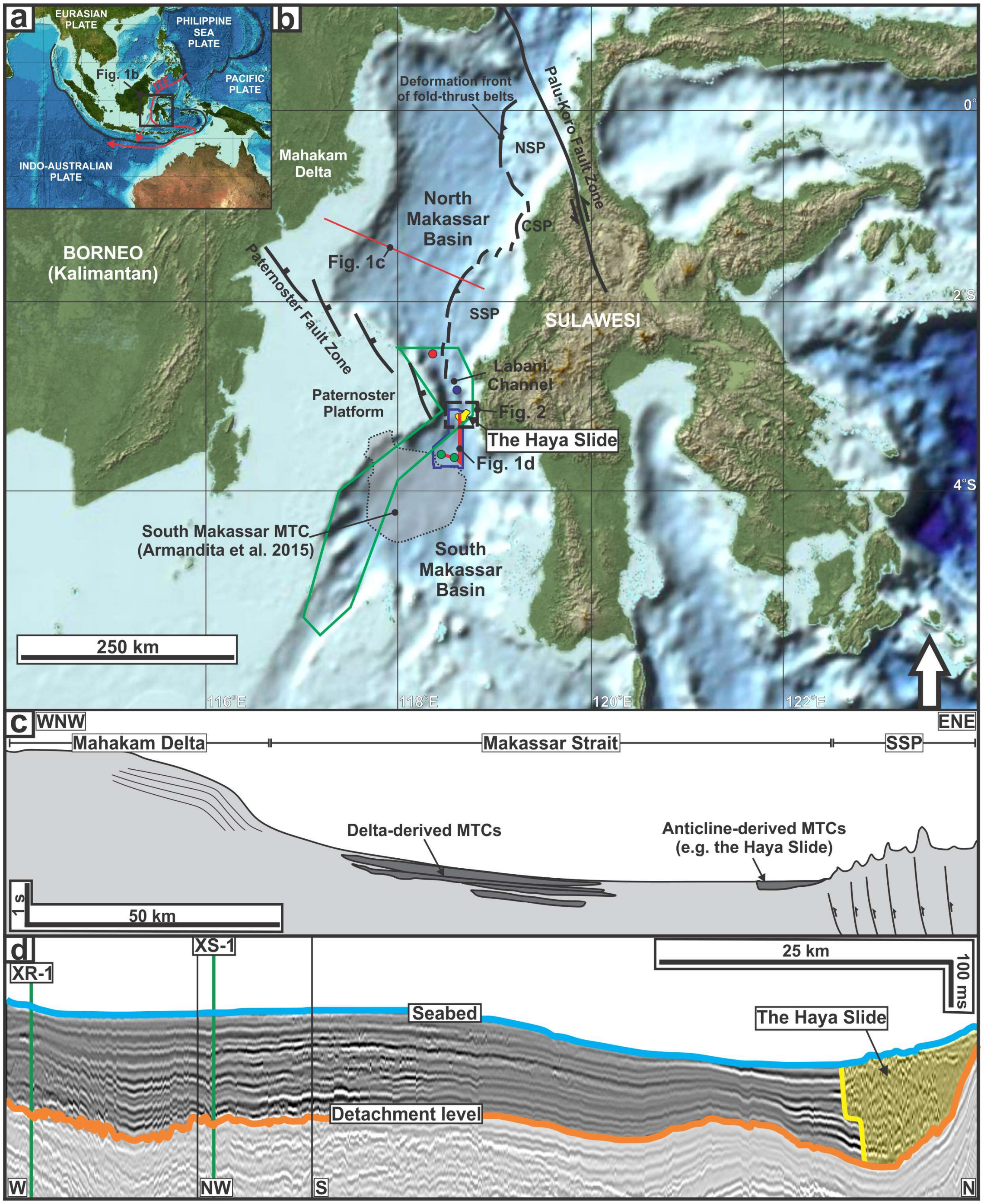
a
EURASIAN PLATE
PHILIPPINE SEA PLATE
PACIFIC PLATE
Fig. 1b
INDO-AUSTRALIAN PLATE
b
Deformation front of fold-thrust belts
Palu-Koro Fault Zone
0°
NSP
Mahakam Delta
North Makassar Basin
CSP
BORNEO (Kalimantan)
Fig. 1c
Paternoster Fault Zone
SSP
SULAWESI
2°S
Labani Channel
Paternoster Platform
Fig. 2
The Haya Slide
Fig. 1d
4°S
South Makassar MTC (Armandita et al. 2015)
South Makassar Basin
250 km
116°E
118°E
120°E
122°E
c
WNW
ENE
Mahakam Delta
Makassar Strait
SSP
Delta-derived MTCs
Anticline-derived MTCs (e.g. the Haya Slide)
1 s
50 km
d
XR-1
XS-1
25 km
100 ms
Seabed
The Haya Slide
Detachment level
W
NW
S
N

Figure 2

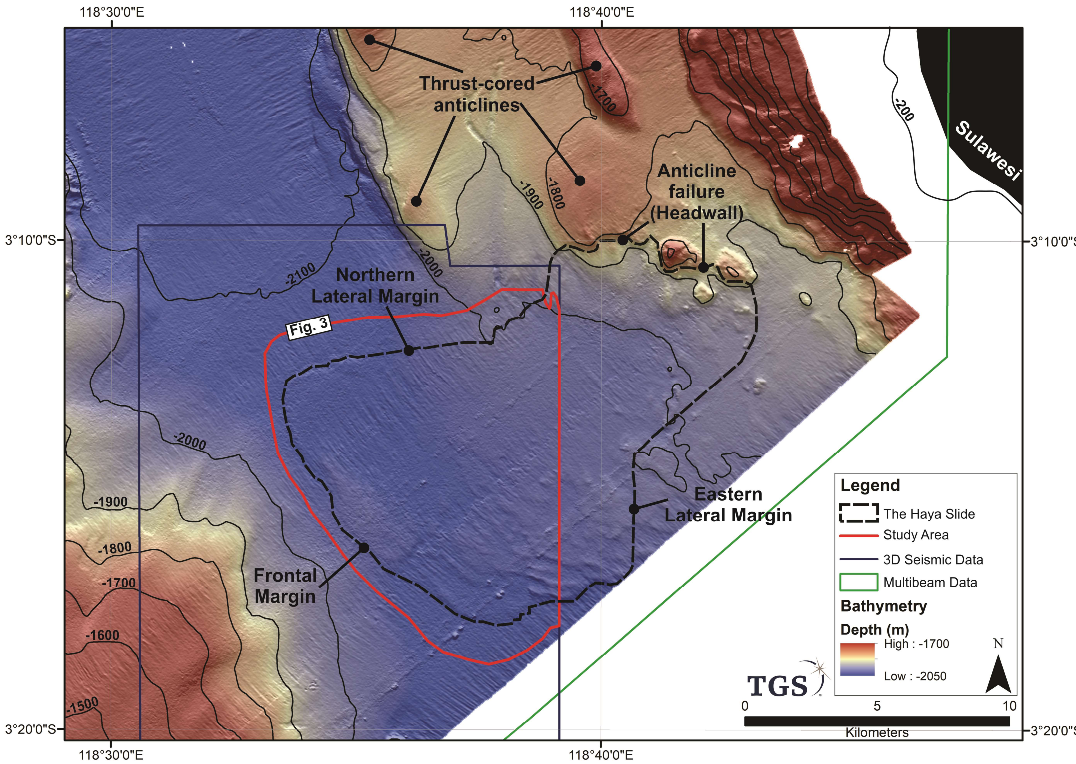
118°30'0"E
118°40'0"E
3°10'0"S
3°20'0"S
Thrust-cored anticlines
Anticline failure (Headwall)
Sulawesi
Northern Lateral Margin
Fig. 3
Eastern Lateral Margin
Frontal Margin
-200
-1500
-1600
-1700
-1800
-1900
-2000
-2100
Legend
The Haya Slide
Study Area
3D Seismic Data
Multibeam Data
Bathymetry
Depth (m)
High : -1700
Low : -2050
N
TGS
0
5
10
Kilometers

Figure 3

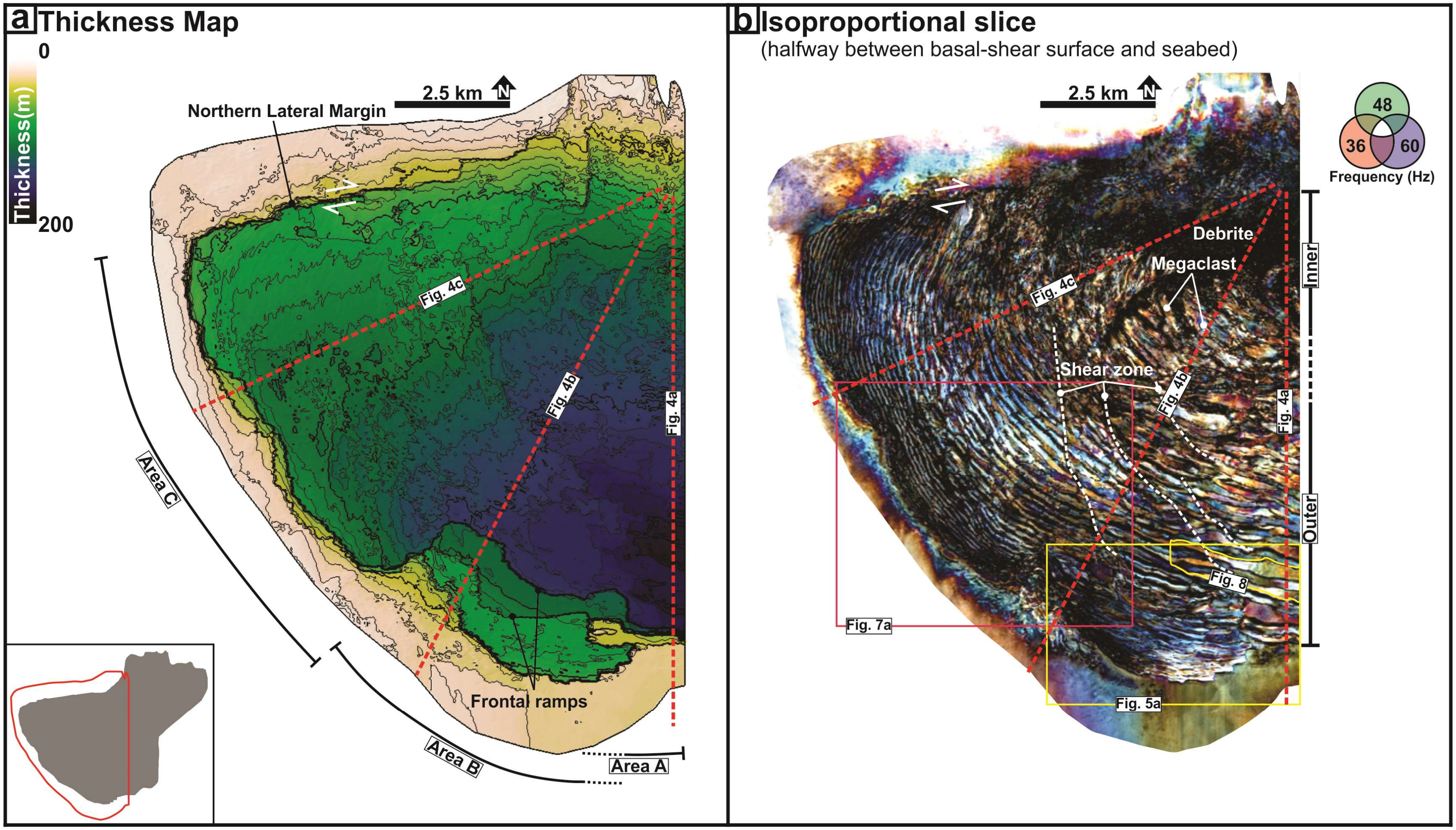
a
Thickness Map
0
Thickness(m)
200
2.5 km
N
Northern Lateral Margin
Fig. 4c
Fig. 4b
Fig. 4a
Area C
Area B
Area A
Frontal ramps
b
Isoproportional slice
(halfway between basal-shear surface and seabed)
2.5 km
N
48
36
60
Frequency (Hz)
Debrite
Megaclast
Fig. 4c
Shear zone
Fig. 4b
Fig. 4a
Inner
Outer
Fig. 8
Fig. 7a
Fig. 5a

1164 Figure 4

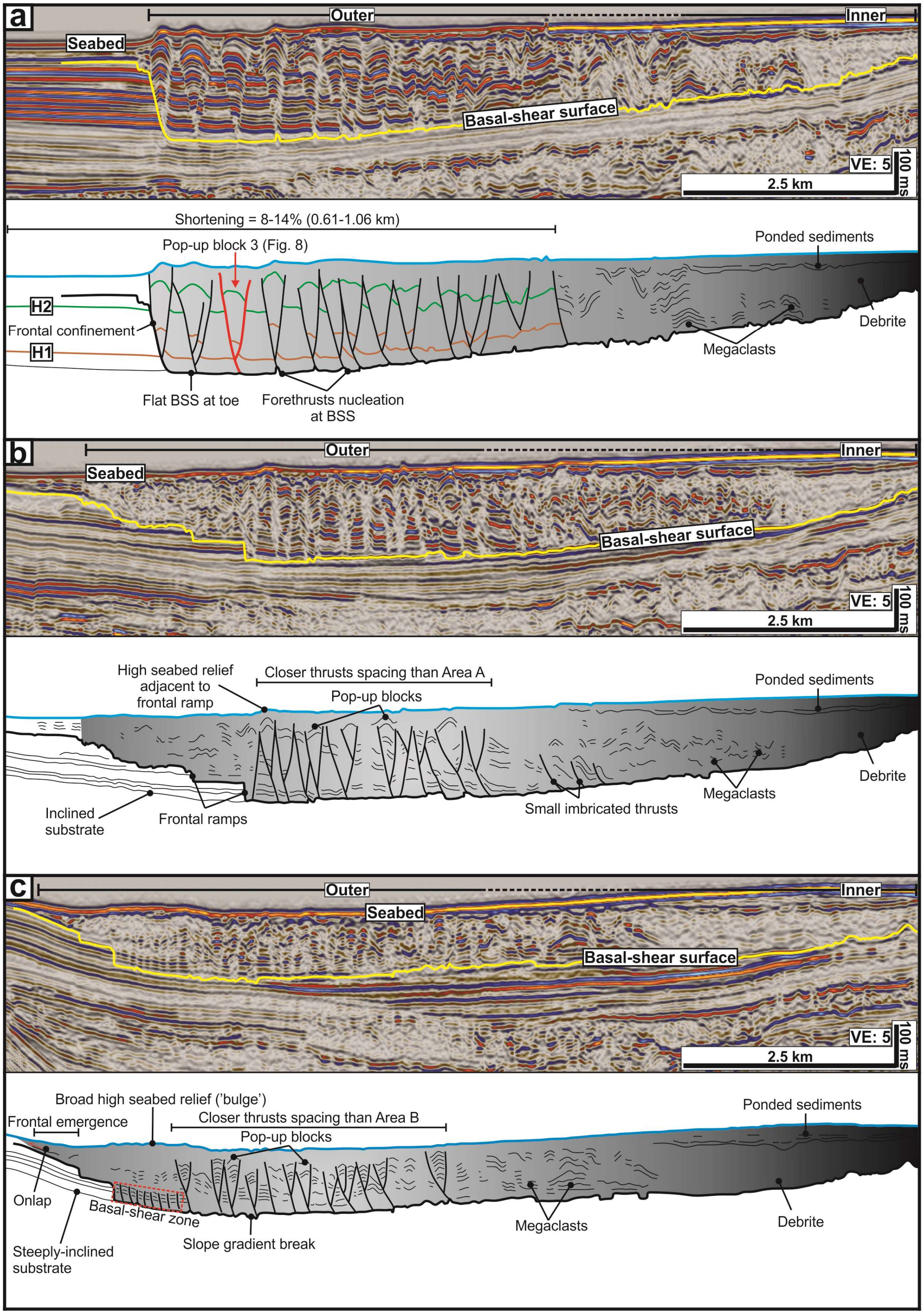

1165

Figure 5

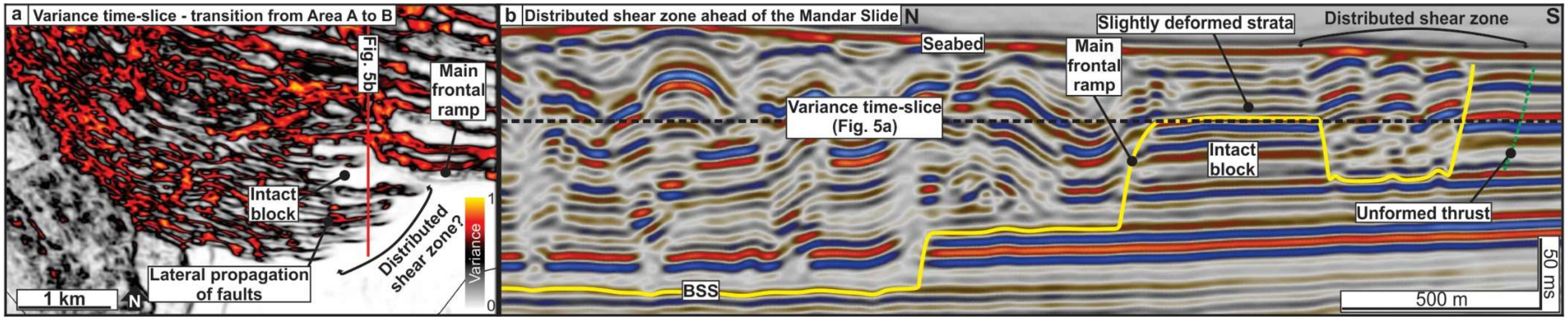
a Variance time-slice - transition from Area A to B
Fig. 5b
Main frontal ramp
Intact block
Distributed shear zone?
Lateral propagation of faults
Variance
1
0
1 km
N
b Distributed shear zone ahead of the Mandar Slide
N
S
Seabed
Slightly deformed strata
Distributed shear zone
Main frontal ramp
Variance time-slice (Fig. 5a)
Intact block
Unformed thrust
BSS
500 m
50 ms

1168 Figure 6

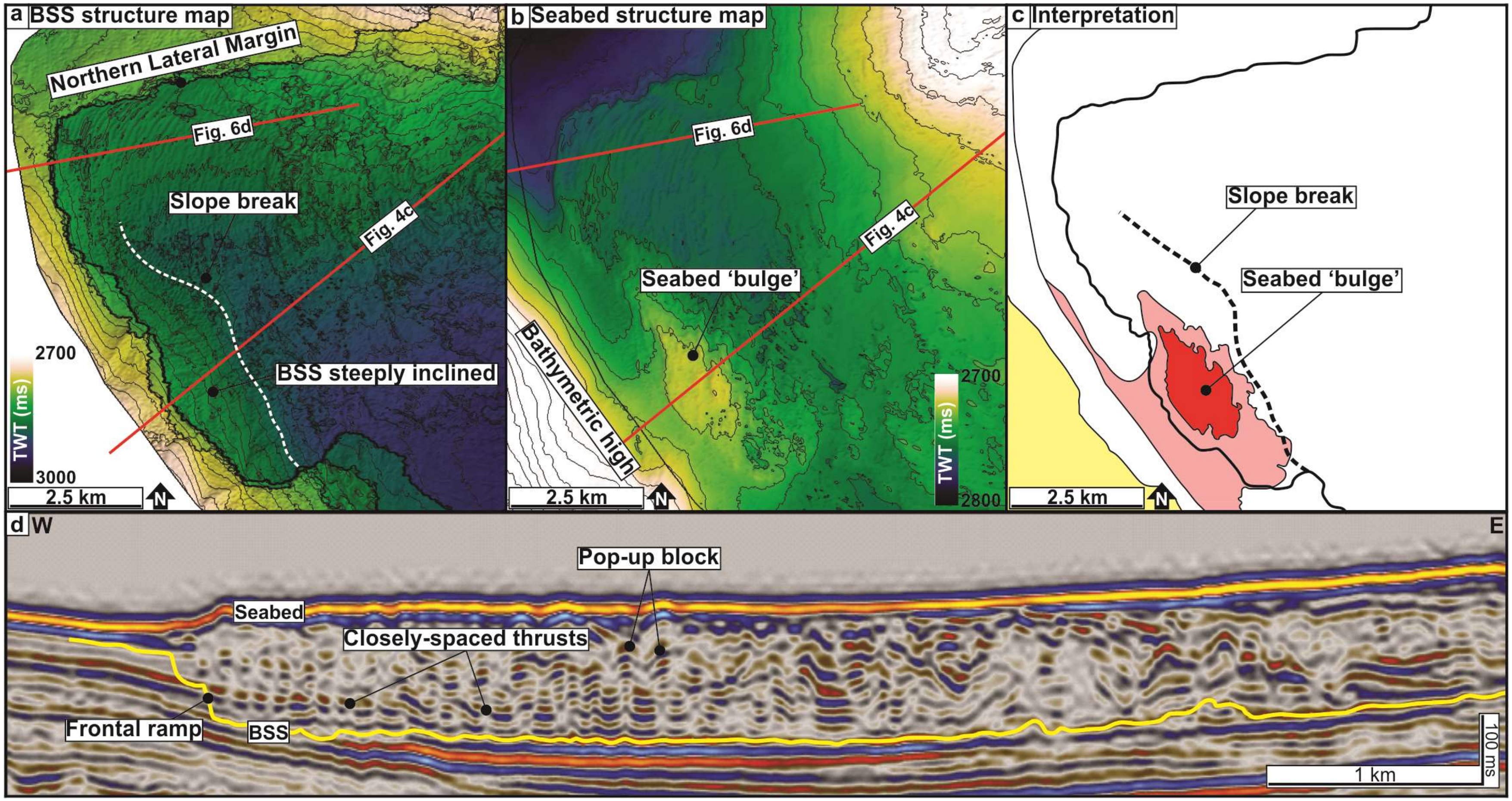

1169

Figure 7

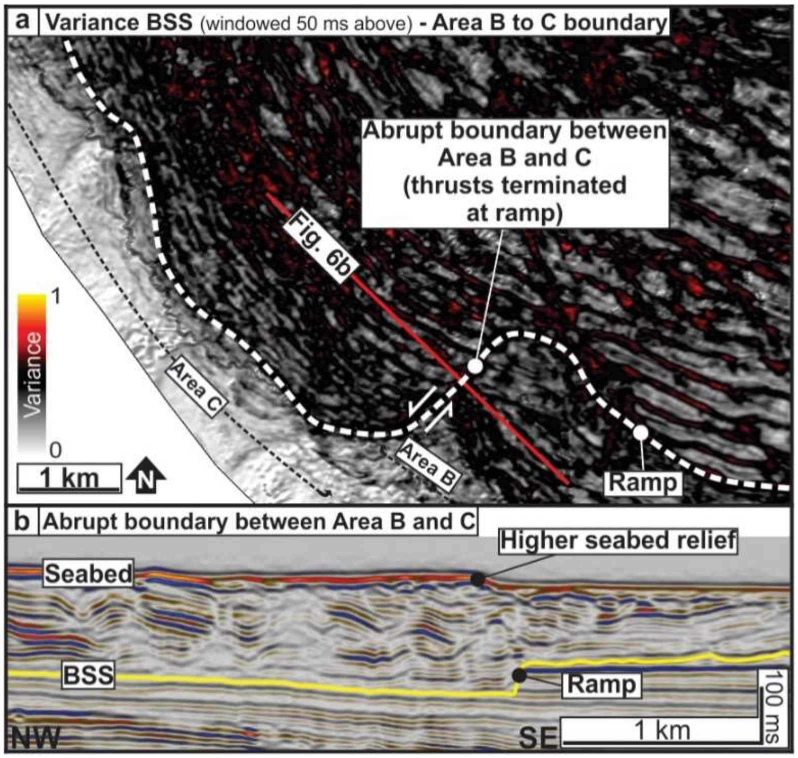

a Variance BSS (windowed 50 ms above) - Area B to C boundary
Abrupt boundary between Area B and C (thrusts terminated at ramp)
Fig. 6b
1
Variance
0
1 km
N
Area C
Area B
Ramp
b Abrupt boundary between Area B and C
Higher seabed relief
Seabed
BSS
Ramp
100 ms
NW
SE
1 km

Figure 8

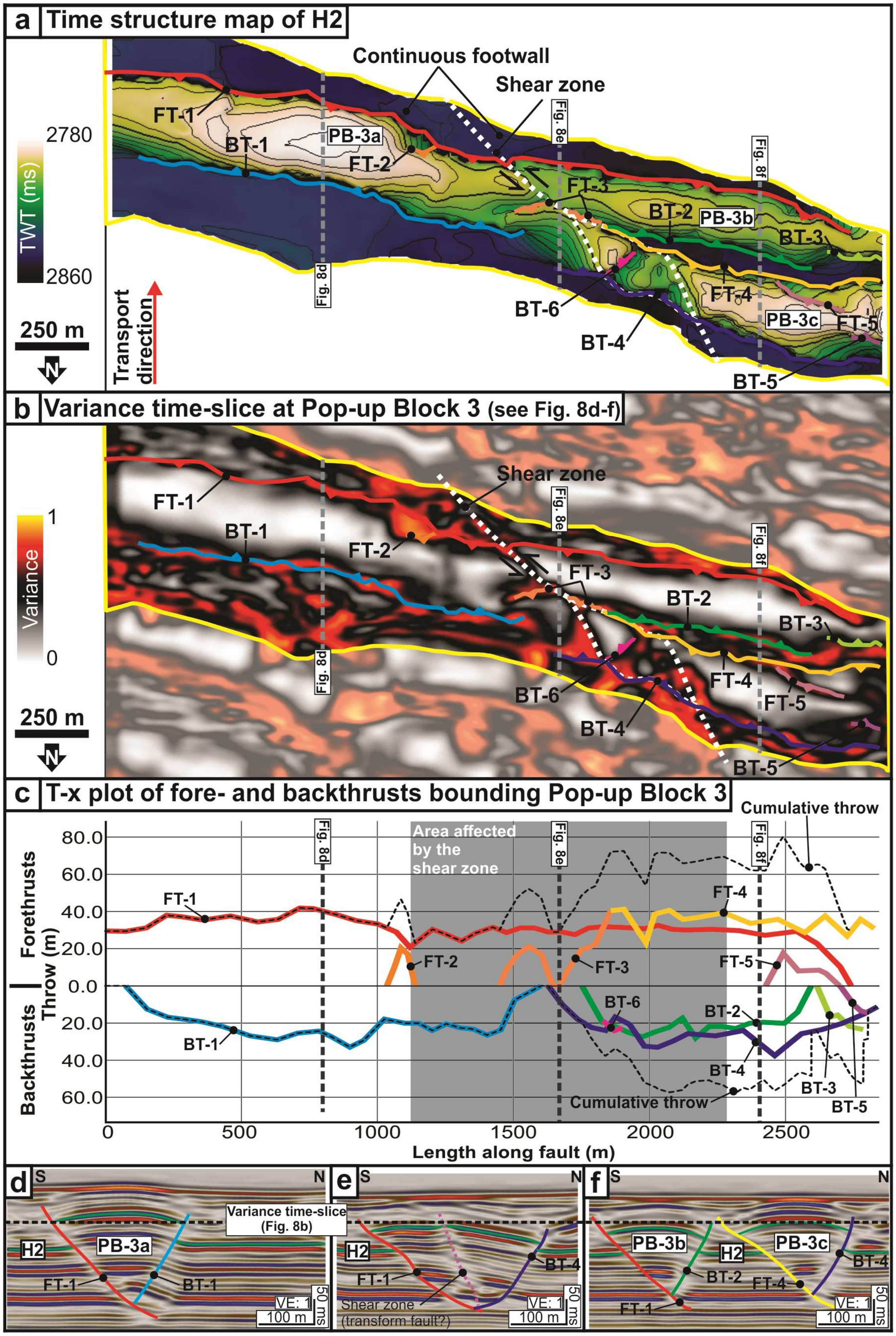

a Time structure map of H2
Continuous footwall
Shear zone
FT-1
BT-1
PB-3a
FT-2
FT-3
BT-2
PB-3b
BT-3
FT-4
PB-3c
FT-5
BT-6
BT-4
BT-5
Fig. 8d
Fig. 8e
Fig. 8f
TWT (ms)
2780
2860
250 m
N
Transport direction
b Variance time-slice at Pop-up Block 3 (see Fig. 8d-f)
Variance
1
0
c T-x plot of fore- and backthrusts bounding Pop-up Block 3
Cumulative throw
Area affected by the shear zone
Forethrusts
Backthrusts
Throw (m)
80.0
60.0
40.0
20.0
0.0
Length along fault (m)
0
500
1000
1500
2000
2500
d S N
Variance time-slice (Fig. 8b)
H2
VE: 1
100 m
50 ms
e S N
Shear zone (transform fault?)
f S N

1174 Figure 9

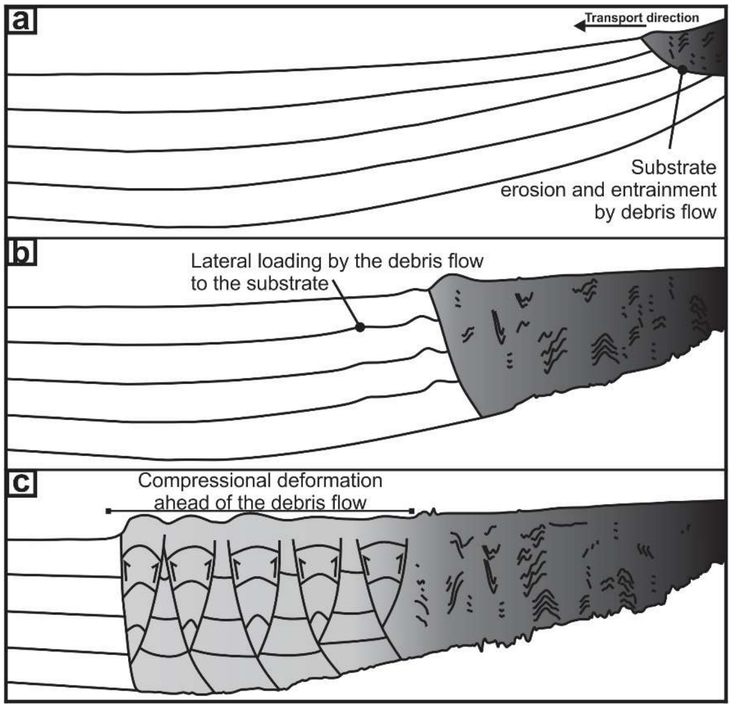

1175

Figure 10

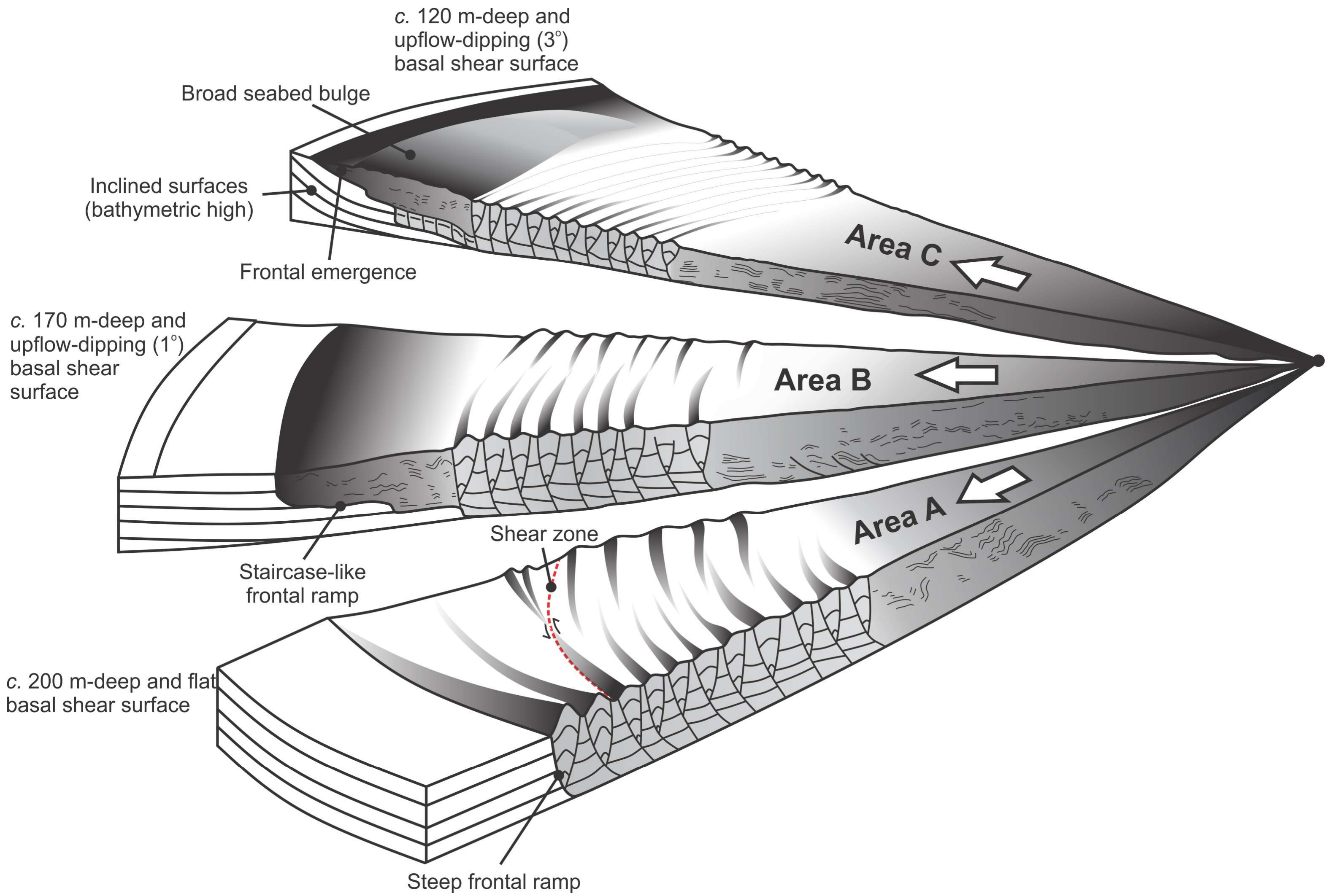

c. 120 m-deep and
upflow-dipping (3°)
basal shear surface
Broad seabed bulge
Inclined surfaces
(bathymetric high)
Frontal emergence
Area C
c. 170 m-deep and
upflow-dipping (1°)
basal shear
surface
Area B
Staircase-like
frontal ramp
Shear zone
Area A
c. 200 m-deep and flat
basal shear surface
Steep frontal ramp

1178 Figure 11

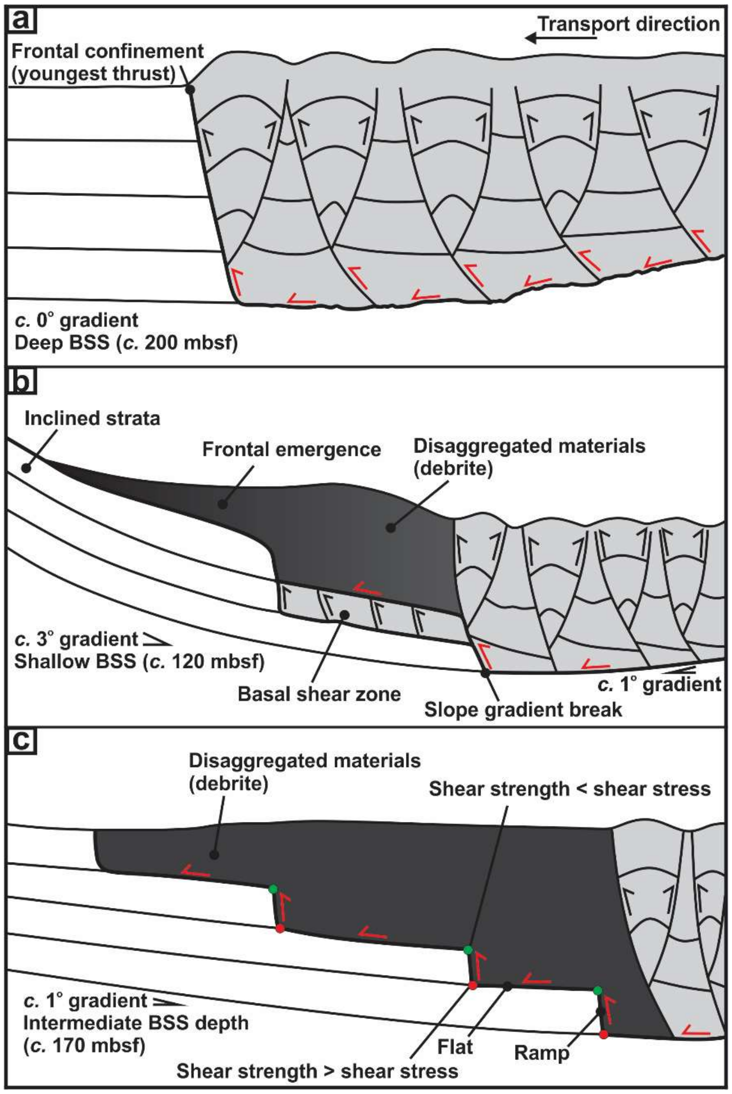

1179

Figure 12

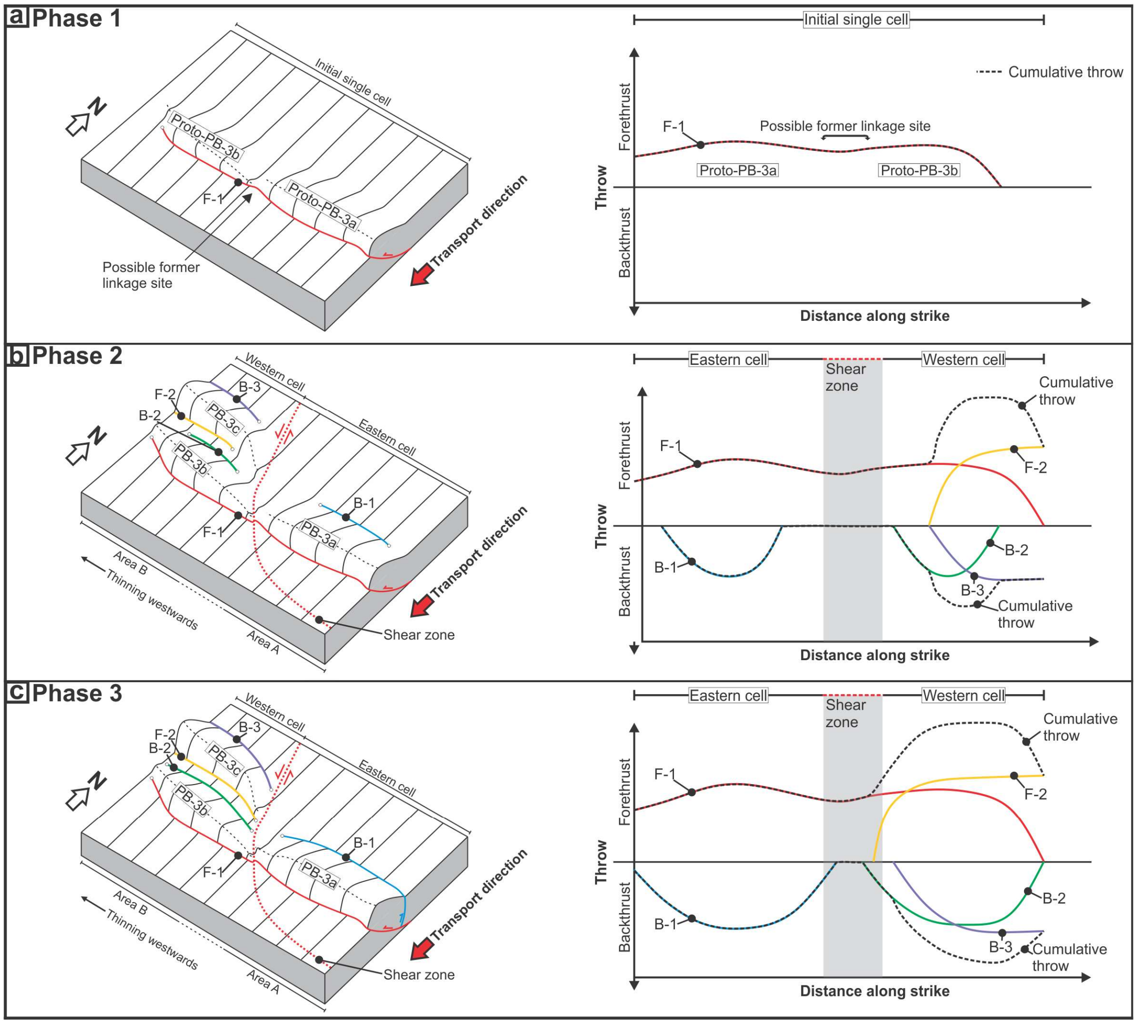
a Phase 1
Initial single cell
N
Proto-PB-3b
F-1
Proto-PB-3a
Possible former linkage site
Transport direction
Initial single cell
Cumulative throw
Forethrust
Throw
Backthrust
F-1
Possible former linkage site
Proto-PB-3a
Proto-PB-3b
Distance along strike
b Phase 2
Western cell
Eastern cell
F-2
B-2
B-3
PB-3c
PB-3b
F-1
B-1
PB-3a
Area B
Thinning westwards
Area A
Shear zone
Transport direction
Eastern cell
Shear zone
Western cell
Cumulative throw
F-2
F-1
B-1
B-2
B-3
Cumulative throw
Distance along strike
c Phase 3
Western cell
Eastern cell
F-2
B-2
B-3
PB-3c
PB-3b
F-1
B-1
PB-3a
Area B
Thinning westwards
Area A
Shear zone
Transport direction
Eastern cell
Shear zone
Western cell
Cumulative throw
F-1
F-2
B-1
B-2
B-3
Cumulative throw
Distance along strike